21GRD02 BIOSPHERE

D2: Report on the determination of the dependence of SCR on PCR and atmospheric parameters (e.g., temperature, density and aerosol concentration) based on the generation of a documented metrological method from field measurement campaigns conducted using the instrumentation from D1.

Organisation name of the lead participant for the deliverable: **PTB**

Due date of the deliverable: **Jun 2025** (M33)

Actual submission date of the deliverable: 30 September 2025

Confidentiality Status: PU - Public, fully open

Deliverable Cover Sheet

Funded by the European Union. Views and opinions expressed are however those of the author(s) only and do not necessarily reflect those of the European Union or EURAMET. Neither the European Union nor the granting authority can be held responsible for them.

European Partnership Co-funded by the European Union

METROLOGY PARTNERSHIP EURAMET

The project has received funding from the European Partnership on Metrology, co-financed from the European Union's Horizon Europe Research and Innovation Programme and by the Participating States.

Glossary

AtRIS	Atmospheric Radiation Interaction Simulator
CME	Coronal Mass Ejection
DECOS	Detector for COSmic radiation
EXPACS	EXcel-based Program for calculating Atmospheric Cosmic-ray Spectrum
FD	Forbush Decrease
GCR	Galactic Cosmic Rays
ICRP	International Commission on Radiation Units and Measurements
ICRU	International Commission on Radiological Protection
IMF	Interplanetary Magnetic Field
JENDL	Japanese Evaluated Nuclear Data Library
LIS	Local Interstellar Spectrum
MCNP	Monte Carlo N-Particle
NRLMSISE	Naval Research Laboratory Mass Spectrometer and Incoherent Scatter Radar
PARMA	PHITS-based Analytical Radiation Model in the Atmosphere
PCR	Primary Cosmic Rays
PHITS	Particle and Heavy Ion Transport code System
SCR	Secondary Cosmic Rays
SEVAN	Space Environmental Viewing and Analysis Network

Contents

1 Summary 3
2 Dependence of SCR on atmospheric parameters 4
2.1 Simulation 6
2.1.1 Atmospheric model 6
2.1.2 Cosmic source definition 8
2.2 Results and discussions 9
2.2.1 Validation of MCNP simulations 9
2.2.2 Relative variation of muon flux and energy spectra with altitude 11
2.3 Correlation analysis 15
3 Correlation of PCR with SCR 20
3.1 Propagation of monoenergetic protons through a standard atmosphere 20
3.2 SCR fluence on the ground 23
3.3 Primary differential energy spectrum 25
3.4 Deducing J_{PCR} from J_{SCR}: parametric forward fitting of the primary spectrum 28
3.5 Matrix formulation of the differential SCR flux 29
3.6 Deducing J_{PCR} from J_{SCR}: The matrix method 30
3.7 Validation of the methodology: comparison with other MC simulation codes and experimental data 31
3.7.1 Comparison with EXPACS 31
3.7.2 Comparison with Forbush decrease measurements 33
4 Conclusion 35
5 Acknowledgments 36
6 References 36

1 Summary

This report presents a methodology to determine the dependence of ground-level secondary cosmic radiation (SCR) on primary cosmic rays (PCR) and atmospheric profiling parameters, specifically air pressure and temperature. This approach integrates ground-based SCR measurements with a simulation model developed using the Monte Carlo N-Particle (MCNP) code. The model incorporates measured atmospheric profiles to simulate the production, absorption, and attenuation of SCR. For this analysis, the study is restricted to ground-level muons, given their

abundance and high penetration power, which make them the dominant contributor to cosmic radiation at sea level.

The accuracy of the MCNP model was validated through comparisons with the PHITS-based Analytical Radiation Model in the Atmosphere (PARMA) and experimental data from field campaigns. The validated model was subsequently applied to investigate the relationship between muon flux and atmospheric pressure. Results reveal a complex dependence, particularly in the troposphere and lower stratosphere, where pressure correlations and barometric coefficients exhibit both positive and negative values as a function of altitude (Al-Qaaod et al., 2025). This method enables the decoding of atmospheric pressure effects from measured SCR flux rates.

Furthermore, the model was used to simulate time-dependent muon count rates, allowing for the determination of the barometric coefficient as a function of altitude. By employing constant pressure and temperature profiles, the dependence of the barometric coefficient on cut-off rigidity was also investigated.

To establish a direct relationship between PCR and SCR, the propagation of monoenergetic PCR protons was studied and the SCR yields per proton were determined. These data facilitate the computation of muon fluence rates at any altitude within the troposphere and enable the deduction of radiation doses at ground level and aviation altitudes.

The overall methodology for correlating SCR with PCR was further confirmed through benchmarking against the EXPACS model, which provides established reference fluxes, and against experimental data collected during geomagnetic storms within the BIOSPHERE project timeline. This dual validation against both a well-tested simulation tool and real-world measurements confirms the model's reliability for capturing both background behavior and disturbance-related variability. Consequently, this work supports critical applications in space weather studies, aviation radiation protection, and environmental monitoring.

2 Dependence of SCR on atmospheric parameters

Secondary cosmic rays arise from the interactions of PCR—predominantly high-energy protons from solar and extraterrestrial sources—with Earth’s atmosphere. These interactions trigger extensive particle cascades, producing protons, neutrons, electrons, muons, and other subatomic particles (Grieder, 2001; Mironova et al., 2015; Gaisser et al., 2016). Among these, muons are particularly prominent due to their high abundance and penetrating ability. Capable of reaching Earth’s surface and even subsurface depths, muons constitute the most readily detectable component of SCR. They are useful across diverse scientific and technological domains, from probing fundamental physics, such as testing quantum chromodynamics models (Albrecht et al., 2022), to practical applications like muon radiography of volcanic structures and muon tomography for nuclear waste monitoring and characterization (Lechmann et al., 2021; Mahon et al., 2019; Thompson et al., 2021).

The high penetrating power of muons, which is due to their small stopping power and the effects of relativistic time dilation (Grieder, 2001; Groom et al., 2001), makes them ideal natural probes for detecting dynamic atmospheric changes over time. Although muons have a rest-frame lifetime of only about 2.2 μs, their velocities near the speed of light extend their observed lifetime in Earth's frame. For example, a 4 GeV muons generated at altitudes of around 15 km can still reach the Earth's surface, as their decay time is dilated by a Lorentz factor $\gamma \approx 39$, allowing them to live long enough—up to ~85 μs in the lab frame—to travel the distance. Continuous monitoring of muon flux at various altitudes could provide real-time insights into the thermal structure of the stratosphere, potentially serving as an indicator of events like sudden stratospheric warming (Tramontini et al., 2019).

The integration of muon data into atmospheric and climate science could open new pathways for understanding the interplay between cosmic radiation, atmospheric chemistry, and climate variability. Muons, as a proxy for cosmic ray activity, can help quantify the ionization rate in different layers of the atmosphere. The observed fluxes can be integrated into atmospheric models to estimate the production of free radicals, their relation to cosmic events (e.g., solar particle events, geomagnetic storms, etc.) and their impact on ozone chemistry.

As muons propagate through the atmosphere, their interactions are influenced by the density distribution of the air (e.g., Winant et al., 2023). As a result, ground-based muon flux measurements capture fluctuations in key atmospheric parameters, primarily pressure and temperature, whereas humidity and aerosol concentration contribute only marginally (Maghrabi et al., 2023). It's well established that air pressure plays a crucial role in observed muon flux rates (Wissmann et al., 2005; Wissmann, 2006). This is because as air pressure increases, the column of air above the detector becomes denser, acting like a shield that reduces the number of muons that can reach the detector. Dealing with the temperature effect on muons is challenging because it depends on how air is spread out at different heights. Higher temperature at high altitudes makes the air expand, causing fewer hadronic interaction of the particles like π- and K-mesons which are the major source of the muons, but also makes muons more likely to decay before they're detected (Wissmann et al., 2005; Tramontini et al., 2019). The overall effect of temperature on muons depends on both how temperature changes with altitude and the energy of the muons. Monte Carlo (MC) simulations, which utilize cross-section data and physics-based models of high-energy particle interactions, combined with vertical atmospheric parameters measured by LIDARs or meteorological radiosondes, enable the separation of atmospheric contributions from genuine cosmic-ray signals. This approach is essential for leveraging muons as a reliable tool for studying atmospheric ionization.

In this work a MCNP model for cosmic ray propagation through the atmosphere, incorporating vertical profiles of pressure and temperature measured by meteorological radiosondes has been developed (Al-Qaaod, 2025). The model predicts the production and transport of various secondary particles, including muons (both positive and negative), neutrons, protons, electrons, positrons, pions (positive and negative, and neutral), kaons (positive, negative, and neutral), and photons, which play a crucial role in assessing cosmic-ray-induced atmospheric ionization and its

impact on atmospheric dynamics. The model was used to decode the pressure effects from the measured muon flux rate during the BIOSPHERE measurement campaign in Brussels (Pierrard et al., 2025). In this section, the focus is placed on validating the model using experimental muon data from a three-month BIOSPHERE measurement campaign in Brussels, together with well-established physical principles. The second part extends the study to correlations between primary and secondary cosmic-ray fluxes. In the present analysis, the barometric effect was chosen as a robust benchmark: the pressure effect on muon flux is immediate and directly proportional to the additional g cm^{-2} of atmospheric overburden (e.g., a pressure swing of ~20 hPa ≈ 20.4 g cm^{-2} over a week leads to a clearly observable ~4% change in flux). To also illustrate the model's sensitivity to temperature, we include simulations comparing summer and winter flux profiles, which demonstrate that the approach captures the seasonal variations associated with the stratospheric temperature (Al-Qaaod et al., 2025). Importantly, temperature profiles are fully incorporated into the simulations, as they are required both for muon production and for correct treatment of the barometric effect. However, short-term variations (day-to-day or over a three-month period) are insufficient to determine a reliable temperature coefficient, since stratospheric temperature effects evolve only on seasonal or synoptic timescales and require at least a full year of data and dedicated correction procedures.

2.1 Simulation

2.1.1 Atmospheric model

The simulation of atmospheric propagation of incoming cosmic rays and their resulting air showers was carried out using the general-purpose ionization radiation transport code Monte-Carlo N-Particle (MCNP) version 6.1, a tool validated for cosmic ray applications (Goorley et al., 2013; Gregg, 2013; Garrett and Gregg, 2014). The atmosphere has been modeled as a rectangular prism extending from sea level to an altitude of 65 km, with a base area of 2 km x 2 km. This prism was divided horizontally into 230 cells to reflect variations in atmospheric conditions, such as density and air composition, see *Figure **1***(a). In this model, the lateral boundaries were treated as void surfaces, allowing secondary particles to exit the volume without reflection. This setup ensures that only particles generated within the atmospheric column or entering from above are tracked.

For the simulation of the atmosphere, radiosonde data (vertical temperature and pressure profiles) over Brussels, provided in the open access database maintained by the University of Wyoming's Department of Atmospheric Science Atmospheric Soundings (https://weather.uwyo.edu/upperair/sounding.html) were utilized [*Figure **1***(b) shows the temperature and pressure profiles for three days in January 2024]. The data for the selected 33 days were used to calculate vertical air density using the ideal gas law up to 26 km altitude. Above that height the density values from the Naval Research Laboratory Mass Spectrometer and Incoherent Scatter Radar (NRLMSISE) model were used, available through NASA's website (https://ccmc.gsfc.nasa.gov/models/NRLMSIS~00/#outputs), tailored to the specific dates and

Brussels' geographical coordinates. The atmospheric data over Brussels was specifically selected because during the time period from January 2024 until March 2024, the 2nd BIOSPHERE measurement campaign to identify and quantify the relationship between cosmic rays, UV radiation and the thickness of the ozone shield was taking place at the urban Brussels region, where two institutes involved in the project, Belgian Institute for Space Aeronomy (BIRA-IASB) and Royal Meteorological Institute of Belgium (IRM-KMI), are located. This campaign involved the simultaneous use of numerous optical instruments such as radiometers, spectrometers and pyranometers for accurate spectral and wavelength-integrated measurements of solar UV irradiance, providing access to UV biologically effective dose rate (UV index), total ozone column and aerosol optical depth, as well as mobile detectors for ground-based secondary cosmic ray measurements (muons and neutrons) (Pierrard et al., 2025). In addition, the campaign was complemented by balloon soundings for vertical profiles of atmospheric parameters, ozone concentration and neutron monitoring, provided by the IRM-KMI, and satellite data on energetic particle fluxes measured by GOES and PROBA-V/EPT, provided by BIRA-IASB.

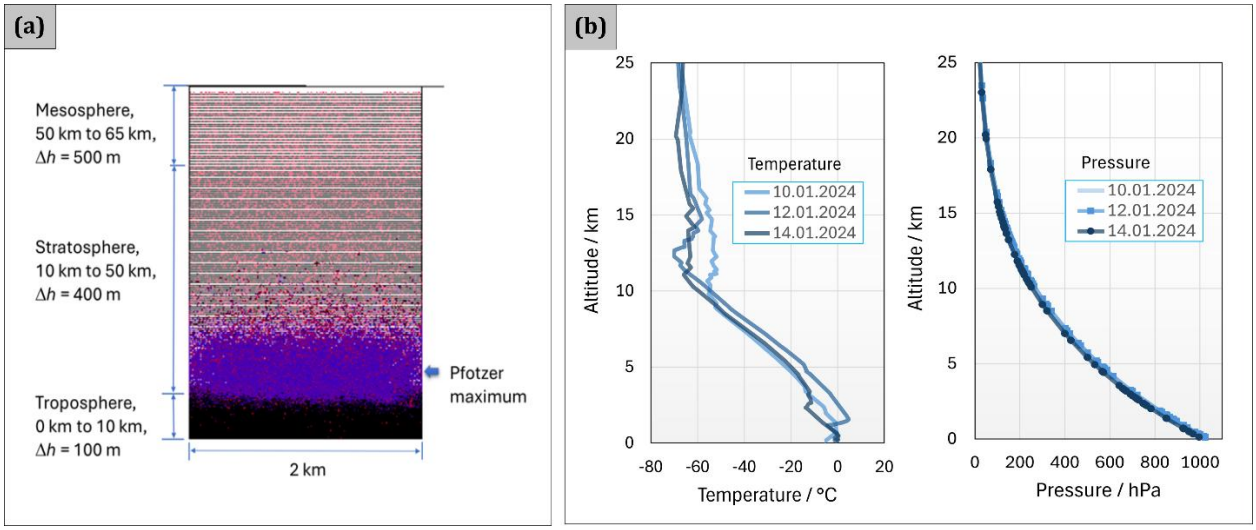

Figure 1: (a) MCNP visualization with the particle display mode showing the schematics of geometry of the atmosphere and distribution of particles. The Pfotzer maximum marks the altitude where the production of secondary particles reaches its peak. (b) Examples of temperature and pressure distribution vs. altitude over Brussels taken from the meteorological sounding database (https://weather.uwyo.edu/upperair/sounding.html).

In the MCNP input file, density profiles for the model's segments were estimated by interpolating values from both the radiosonde measurements and the NRLMSISE model, to ensure matching with the altitudes of the layers in the atmospheric model (Al-Qaaod et al., 2025). At this stage, the atmosphere's composition in the material card was assumed to be uniform across all altitudes, consisting of 75.53% nitrogen, 23.18% oxygen, 1.28% argon, and 0.01% carbon dioxide by weight (carbon dioxide is converted into its elemental composition, carbon and oxygen, in the material card). The simulation of the atmospheric propagation of high-energy cosmic rays and their cascades utilized MCNP's data libraries and physics models, covering particle energies ranging from approximately 0.1 GeV/n to 1000 GeV/n. For neutron- and proton-induced reactions, the

extended version of Japanese Evaluated Nuclear Data Library (JENDL) Version 4.0 (up to 200 MeV) was chosen, known as JENDL-4.0/HE. For modeling interactions at intermediate and high energies, we employed the intra-nuclear cascade (INC CEM) and the Los Alamos version of the Quark-Gluon String Model (LAQGSM), respectively.

2.1.2 Cosmic source definition

The most recent MCNP definition of cosmic ray source available in the code includes automatic source normalization, solar modulation, and geomagnetic rigidity cutoff (R_c) of galactic cosmic ray (GCR) spectra (McKinney *et al.*, 2012) . The solar modulation potential is integrated into the cosmic ray source and is set to a specific date with the DAT keyword using the parameterized data. The source generates the energy spectrum of protons and alpha particles at 65 km altitude, based on the date and Earth's location. Since protons and alpha particles constitute 99% of primary cosmic rays, it is reasonable to assume that only these particles contribute to the generation of secondary cosmic rays. *Figure **2*** shows the proton spectra for the selected date of January 1st, 2024, which is close to the maximum solar activity of the current solar cycle (designated as Solar Cycle 25), at five different locations in the northern hemisphere, including the cities of Oslo (R_c≈ 1.4 GV), Braunschweig (R_c≈ 2.9 GV), Brussels (R_c≈ 3 GV), Athens (R_c≈ 8 GV), and Riyadh (R_c≈ 14 GV). The figure shows the progressive clipping of the low-energy galactic spectrum as one moves from low R_c (Oslo), where the magnetic field lines are more perpendicular to the Earth's surface, to high R_c (Ryiadh), where the field lines are more parallel to the surface, impeding the entry of cosmic rays into the Earth atmosphere compared to the poles.

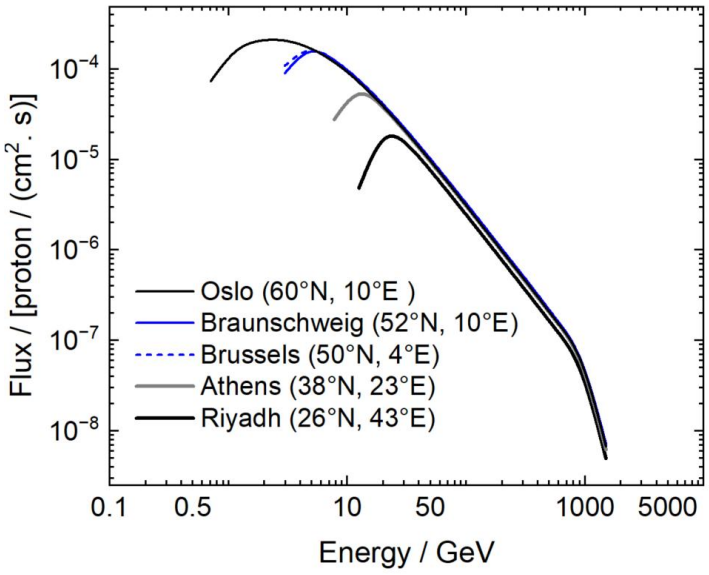

Figure 2: Proton spectra on January 1st, 2024 at different latitudes showing the effect of cutoff-rigidity on the primary spectrum.

2.2 Results and discussions

2.2.1 Validation of MCNP simulations

In this study, 33 input files were run, each corresponding to the vertical pressure and temperature profile of a selected day within the 2nd BIOSPHERE campaign (January 2024 to March 2024), see Al-Qaaod et al. (2025). These particular 33 days were chosen due to the notable structures in the observed muon flux. In all input files, 18 particle types were set in the model card and simulated for transport. These include: neutrons, photons, protons, deuterons, tritons, electrons, positrons, muons (μ^- and μ^+), pions (π^+, π^-, and π^0), kaons (K^+ and K^-), anti-protons, anti-neutrons, helium-3 nuclei (^{3}He), alpha particles (^{4}He), and heavy ions. The fluxes of neutrons, muons, protons, electrons, alpha particles, pions, and kaons were scored at 24 different altitudes using the flux-over-a-surface tally. The number of source-particle histories for each of the calculations was 10^9, which resulted in a relative statistical uncertainty of <0.05%. The 33 input files correspond to one file per day, each representing the daily atmospheric profile. The atmospheric pressure and temperature data were obtained from radiosonde measurements at Beauvechain Air Base, Belgium (WMO station 06458, ICAO EBBE). These observations are recorded once daily at 00:00 UTC, providing vertical profiles from the surface to the upper atmosphere. Therefore, the temporal resolution of our atmospheric input data is daily, and the spatial resolution corresponds to the vertical resolution of the radiosonde measurements.

The barometric effect significantly influences the muon flux observed on the ground and is crucial for disentangling cosmic effects from atmospheric artifacts. The current MCNP model was validated using experimental muon data obtained with the PTB's mobile muon detector DECOS2 (DEtector for COSmic radiation 2) during 33 days from January 5th to February 15th, 2024. DECOS2 is a new version of the PTB reference detector DECOS1 (Krasniqi et al., 2022), consists of two scintillator-based detection units, each with a 2-dimensional spatially sensitive readout. Each unit contains two crossed layers, each composed of ten EJ-200 plastic scintillators bars (50 cm long, 5 cm wide and 1 cm thick). This arrangement of scintillator bars, in combination with quadruple coincidence detection (one for each scintillator layer), enables position-sensitive detection with a pixel size of 5 cm x 5 cm. The units can be rotated in space and their separation can be adjusted. The variable distance between the two detector units allows for an adjustable field-of-view (FOV) of the detector. *Figure **3*** compares the muon flux measured on the Brussels urban site with one simulated using the MCNP model and vertical atmospheric profiling parameters over Brussels (radiosonde data). Simulations compare well with the measured data, with a the reduced c-square (c-square per degree of freedom) $\chi^2_\nu = \sum_i \left[(O_i - E_i)^2 / \left(\nu \cdot \sigma_i^2\right)\right] \approx 0.33$, with O_i being the measured muon flux, E_i the simulated muon flux, σ_i the uncertainty of the measured data and ν the degree of freedom (ν=33). For the MCNP6 simulation points in , the error bars represent the statistical uncertainties reported by MCNP6 for each tally. MCNP6 provides the relative statistical error R for each result, which we converted to an absolute error via: $(\sigma_{total} = Flux \times R)$. Positive ($\mu^+$) and negative ($\mu^-$) muons were simulated separately, and their uncertainties were propagated to obtain the total muon flux uncertainty

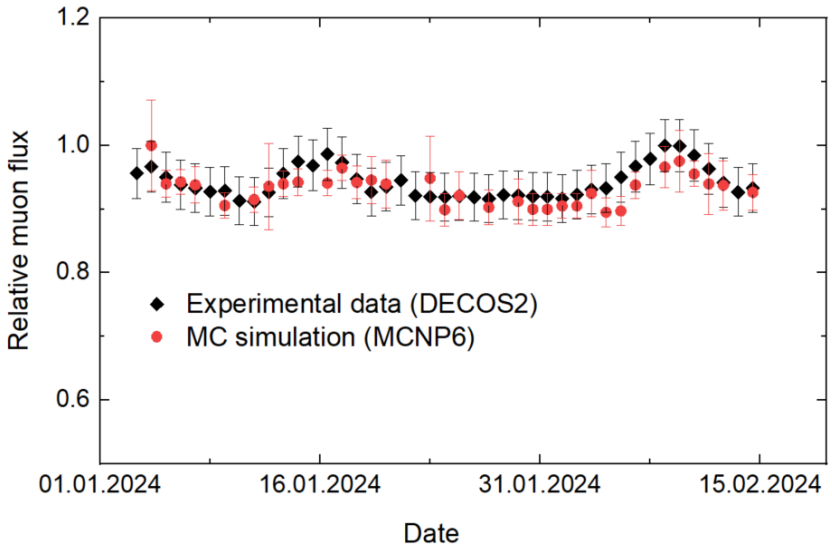

Figure 3: Comparison of the muon flux measured during the 2nd BIOSPHERE measurement campaign in Brussels with the muon flux calculated with the MCNP model, both fluxes normalized to the maximum value. The simulation model was fed with vertical atmospheric profiles over Brussels, which were measured during the campaign with meteorological radiosonde.

Muon spectra simulated using MCNP model were also compared with those from the PHITS-based Analytical Radiation Model in the Atmosphere (PARMA), which was validated using multiple sets of experimental data at nearly the same location and altitude (Sato, 2015, 2016). *Figure **4*** shows the comparison of muon plus (μ^+) spectra simulated using the MCNP model and PARMA as implemented in EXcel-based Program for calculating Atmospheric Cosmic-ray Spectrum (EXPACS) for the selected altitude of 0.2 km and location (cutoff rigidity) at ~ 8 GV. One can observe the good agreement between the two, although minor discrepancies between MCNP and PARMA are likely due to the different models employed. In MCNP, the Cascade-Exciton Model (CEM) physics model is used for intermediate energy interactions, and LAQGSM for high energy scenarios. Additionally, atmospheric densities and temperatures in MCNP are derived from actual radiosonde measurements up to an altitude of about 26 km. Above this altitude, density values from the NRLMSISE model are used. Conversely, in the PARMA model, densities and temperatures are based on the US Standard Atmosphere 1976. Furthermore, while PARMA considers Galactic Cosmic Ray (GCR) protons and heavy ions with charges up to 28 (Ni) as source particles, MCNP only accounts for proton and alpha spectra.

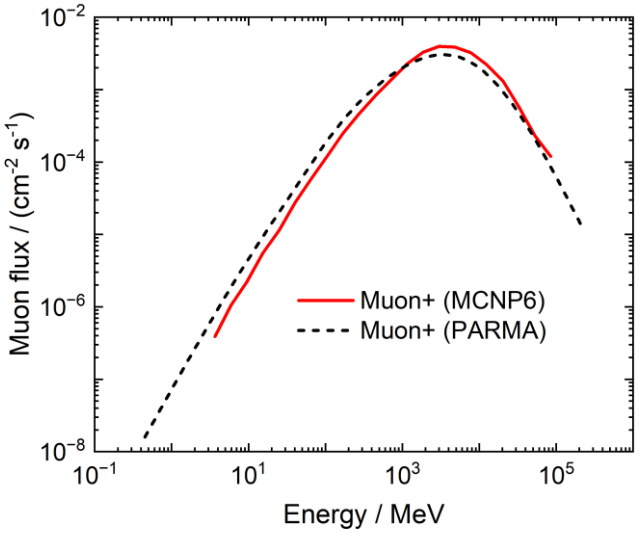

Figure 4: Comparison of the positive muon spectra calculated with MCNP (this study) and PARMA (Sato, 2015), at an altitude of 0.2 km and a cutoff rigidity of 8 GV. In both cases, the muon spectrum at this altitude peaks at about 4 GeV.

2.2.2 Relative variation of muon flux and energy spectra with altitude

In the simulation, the muon flux was scored at 24 height levels, from the ground surface up to a height of 25 km. The initial altitudes were set to 0 km, 0.1 km, 0.2 km, 0.5 km, 1 km, 3 km, 5 km, 7 km and 10 km, while for the remining altitudes the step size was varied between 0.8 km and 1 km. All muon flux values presented in this work are normalized to their respective maximum values to highlight relative variations with altitude, season, and atmospheric conditions (Al-Qaaod et al., 2025). In *Figure **5***, the values are shown for selected days at various altitudes, alongside the corresponding vertical atmospheric temperature profiles. Each curve corresponds to a different day and illustrates the muon flux variation with temperature across altitudes. Starting from an altitude of about 25 km, the results show the peak at about 15 km, which is known as the Pfotzer maximum (Grieder, 2001). Beyond this point, at lower altitude, absorption and decay of muons start to take over and the muon flux begins to reduce. Both pressure and temperature profiles are essential inputs to the simulation in order to predict the muon flux at ground level. Pressure determines the total atmospheric overburden that muons must traverse, while temperature modifies the altitude–density profile of the atmosphere and thereby shifts the effective production height of muons. The upward shift of the muon production layer, Δh, can be approximated as $\Delta h \approx h_0 \cdot \Delta T/T_0$, where h_0 is the mean production altitude at temperature T_0 [Wissmann, Dangendorf, and Schrewe (2005)]. For example, if h_0=12 km and $\Delta T/T_0$=4%, the production layer Δh rises by about 500 m. This additional distance is significant: muons with energies around 1.9 GeV, which are already close to their decay threshold, would not survive the extra path length and therefore would not reach the ground.

For temperature effects to become clearly visible in muon data, two conditions must be met: (a) sufficiently large variations in the effective temperature, which is a weighted average stratospheric

temperature that indicates how favorable the atmosphere is for pions and kaons to decay into muons instead of reinteracting (typically on the order of 10 K to 15 K), and (b) a consistent temporal trend. During January and February 2024 datasets (see *Figure **5***(a)), for instance, the effective temperature variations are typically below 6 K, with only occasional increases up to ~12 K. Such fluctuations are often masked by barometric pressure changes and by statistical uncertainties in the muon counting rate, making it impossible to extract a reliable temperature coefficient during the time the experiment campaign was carried out. Ground-level temperature variations do not play a role, since muons are produced much higher in the atmosphere. It is the stratospheric temperature that matters, and this evolves only on seasonal or synoptic time scales. That's exactly what is observed in muon seasonal modulation studies [Wissmann, Dangendorf, and Schrewe (2005); Arunbabu et al. (2017)].

In the present work, the influence of temperature expressed through the temperature coefficient has not been isolated from pressure effects. To nevertheless illustrate the model's sensitivity to temperature and the importance of including realistic temperature profiles in the simulations, we have performed simulations for both summer and winter conditions. The corresponding results (see *Figure **5***(b)) demonstrate that the model captures the seasonal changes associated with the effective temperature. To make these subtle seasonal differences clearer, *Figure **6*** shows the flux ratio $\Phi_{winter}/\Phi_{summer}$ as a function of altitude. The results reveal that the muon flux is slightly higher in winter than in summer at lower altitudes (below ~12 km). This is explained by the upward shift of the production layer in summer: muons must travel a longer distance to reach the ground, and more of them decay in flight. Consequently, the ground-level muon flux in winter is about 3.6% higher than in summer, in good agreement with the measurements reported by Wissmann, Dangendorf, and Schrewe (2005).

*Figure **5***(b) also presents muon flux profiles simulated using AtRIS (Atmospheric Radiation Interaction Simulator; Banjac et al., 2019a,b; Winant et al., 2023), with protons and alpha particles as primary inputs. The same atmospheric profile used in the MCNP simulations was applied in AtRIS; however, the atmosphere was extended to 100 km altitude and discretized into 200 layers, each 500 meters thick. The recommended GEANT-4 physics list for AtRIS was used (Winant and Pierrard, 2025; Winant, Pierrard and Botek, 2025). Primary particle energies ranged from 1 MeV to 1 TeV, distributed across 120 energy bins. To compute the muon flux, the galactic cosmic ray spectrum was derived using the Force Field Approximation, based on the local interstellar spectrum (LIS) from Herbst et al. (2017), with a modulation potential of φ = 820 MV corresponding to January 1, 2024. The resulting muon profiles qualitatively agree with those obtained from the MCNP model for both summer and winter conditions, with minor quantitative differences (up to 7%) attributable to differing assumptions between the two simulation approaches.

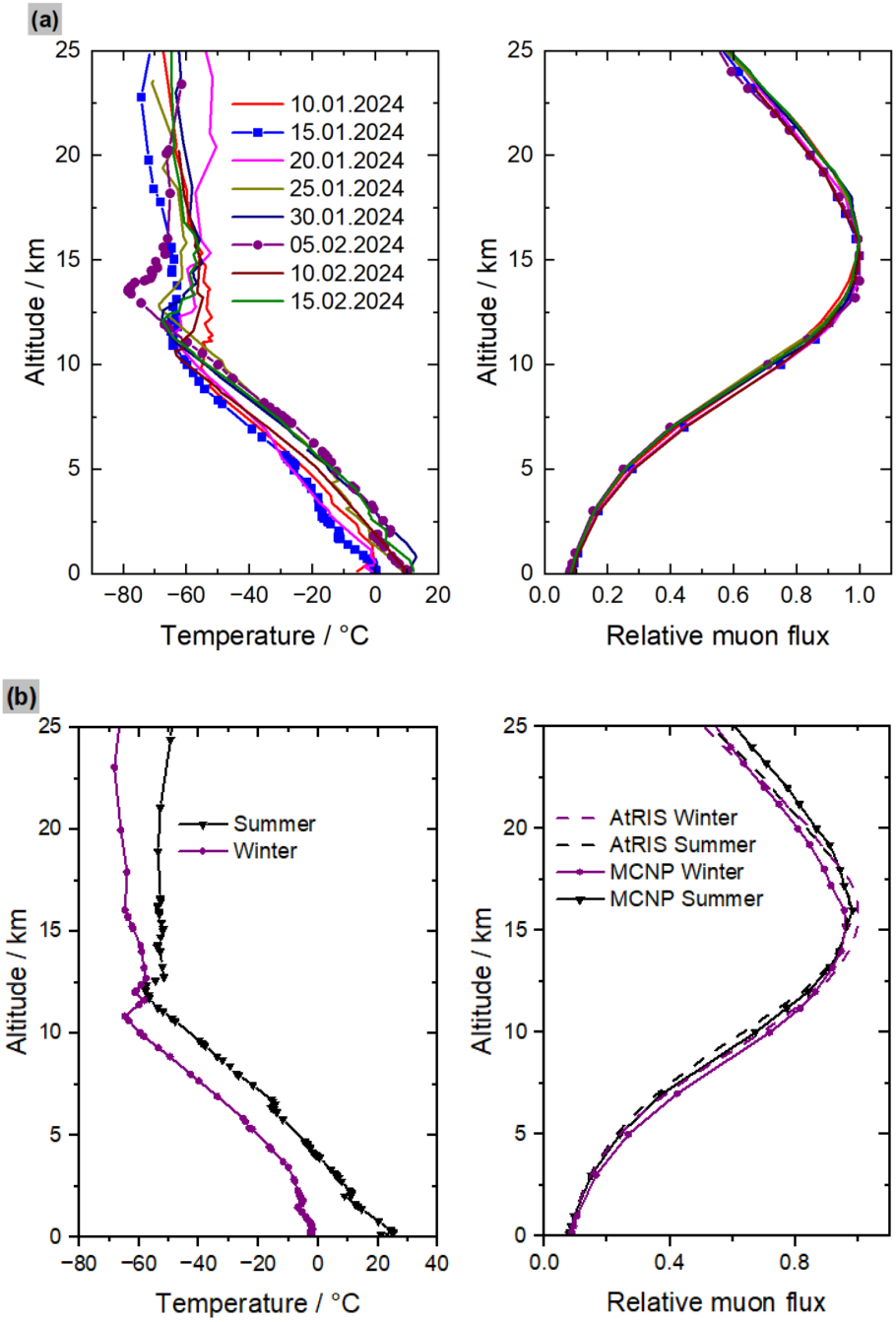

Figure 5: (a) Variation of the measured atmospheric temperature and simulated muon flux with altitude. The temperature profiles represent measurement with radiosondes during selected days in winter. (b) Seasonal (summer and winter) variations in atmospheric temperature and the corresponding normalized muon flux with altitude. The results of AtRIS for summer and winter profile of 2024 are also illustrated for comparison.

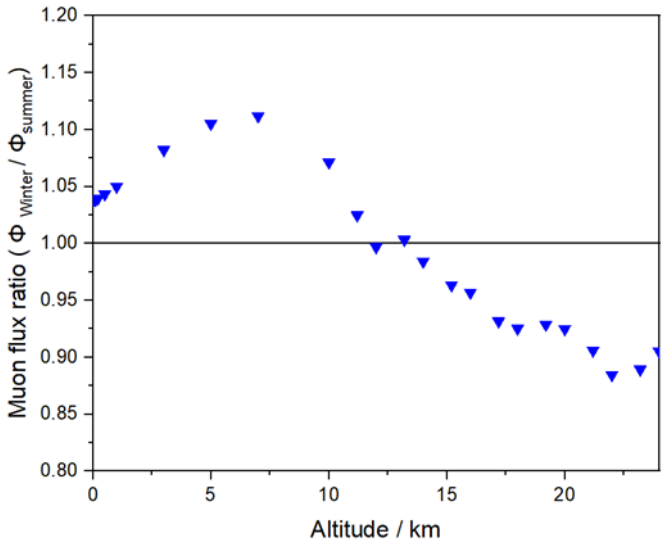

Figure 6: Ratio of simulated muon flux in winter to summer (Φ_{winter} / Φ_{summer}) as a function of altitude. A value greater than 1 indicates higher muon flux in winter, while values below 1 indicate higher flux in summer.

The effects of absorption and decay are best illustrated in the muon spectra presented in *Figure* **7**. Energy spectra for both positive and negative muons were scored at various altitudes for the atmospheric profiles over Brussels corresponding to 15 January 2024. The figure demonstrates a progressive shift in the peak of the muon distribution, from approximately 0.7 GeV at the Pfotzer maximum to around 4 GeV at an altitude of 100 m. This shift is accompanied by a significant decrease in muon flux, which drops by more than an order of magnitude from 15.2 km to 0.1 km. While muons lose energy as they traverse the atmosphere, the flux at lower altitudes is dominated by higher-energy muons, which are less likely to decay due to time dilation effects, allowing them to penetrate deeper into the atmosphere. In contrast, lower-energy muons are more likely to decay before reaching these altitudes, contributing to the observed upward shift at higher altitudes. The charge asymmetry in cosmic ray-induced muons arises because cosmic rays, which are mostly high-energy protons, collide with atmospheric nuclei and preferentially produce more positively charged mesons, pion plus (π^+) and kaon plus (K^+), than their negative counterparts.

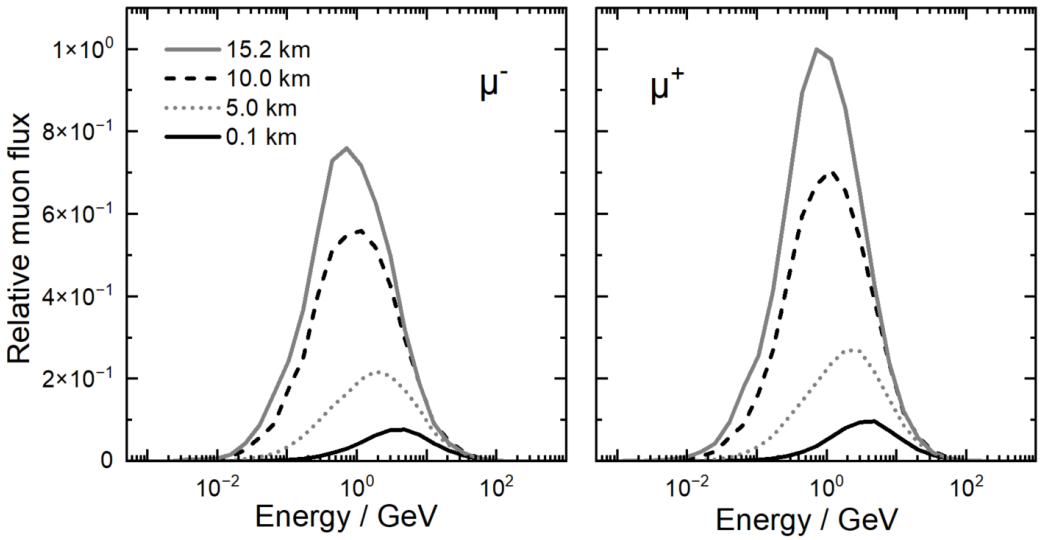

Figure 7: Simulated energy spectra of negative and positive muons scored at four different altitudes.

2.3 Correlation analysis

The SCR flux measured on the ground is intrinsically linked to the flux and energy spectrum of primary cosmic radiation (Gaisser et al., 2016). While PCR initiates the production of SCR through nuclear interactions in the atmosphere, the resulting SCR flux is modulated by atmospheric parameters such as pressure and temperature, solar activity, and geomagnetic effects (Grieder, 2001). Although the correlation of SCR flux with these effects is established to a considerable degree, refining the empirical models relating SCR flux observed on the ground with atmospheric parameters would enable incorporating real-time atmospheric data to improve the accuracy of SCR predictions, but also to use SCR fluxes as a data channel for climate science.

Variation in the atmospheric pressure and temperature can cause considerable changes in the muon flux measured on the ground. To compare measurements taken at different times or locations, these pressure-induced variations must be accounted for. This will allow separation of atmospheric effects from the genuine cosmic ray variations such as Forbush decrease or ground level enhancements. *Figure **8*** presents the raw muon and neutron count rates measured during the BIOSPHERE campaign in Brussels using PTB's muon detector DECOS2 and the neutron monitor in Dourbes, which is part of the Real-time Neutron Monitor Database (NMDB) (Mavromichalaki et al., 2011), https://www.nmdb.eu/nest/. In both cases, a clear anticorrelation with atmospheric pressure is observed. A pressure decrease of approximately 40 hPa results in an increase of more than 8% in the muon count rate and over 27% in the neutron count rate. Pressure changes dominate the effect of atmosphere in the measured muon flux due to their influence on atmospheric density and cosmic ray interaction probabilities.

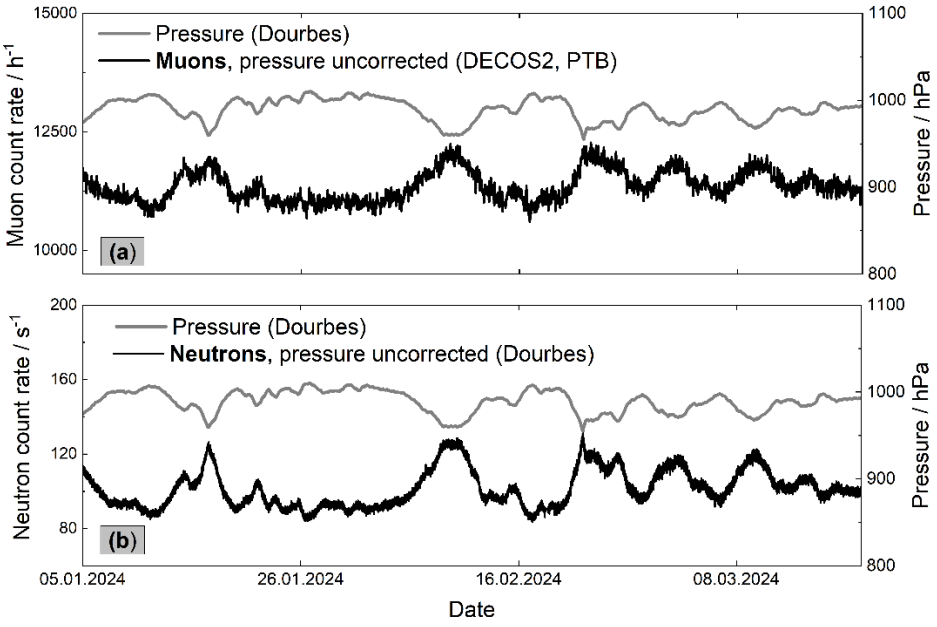

Figure 8: Anticorrelation of the SCR flux with atmospheric pressure. (a) Muons measured with DECOS2 during the Brussels measurement campaign and (b) neutrons measured with the neutron monitor in Dourbes, which is part of the real-time NMDB.

Temperature, while less significant, introduces additional variability, especially in the stratosphere. The temperature dependence of SCR flux is more complex than that of pressure. An increase in temperature typically lowers the air density. When this happens in the stratosphere, this leads to the upward expansion of the air and the rise of muon production layer. Temperature changes in the troposphere, on the other hand, are more related to the absorption of muons through air density changes and are often intrinsically encoded in the pressure effects (e.g., during air mass movements). Here we explore only correlation effects related to pressure.

*Figure **9*** shows the muon flux scored at different altitudes, from 0.1 km to 16 km (Al-Qaaod et al., 2025). Each simulation data point represents the relative flux rate over Brussels, with atmospheric profiles (pressure and temperature) from radiosonde measurements taken over the same location. The maximum flux value at 16 km was used as the reference for normalizing the muon flux values at all altitudes in *Figure **9***. This common normalization standard ensures direct comparability across different altitudes. The absolute value of the reference flux used for normalization was 0.12836 $cm^{-2}s^{-1}$. *Figure **10*** shows the same data, plotted as muon flux versus atmospheric pressure, together with their linear fits obtained using ordinary least squares (OLS) regression and the corresponding relative uncertainties. From both Figures it is evident that below 10.5 km, atmospheric pressure is well anticorrelated with the muon flux, as expected and measured. At higher altitudes, however, a positive correlation appears between atmospheric pressure and muon flux. This relationship is illustrated in *Figure **11***, which displays the Pearson correlation coefficient for muon flux and atmospheric pressure up to an altitude of 20 km.

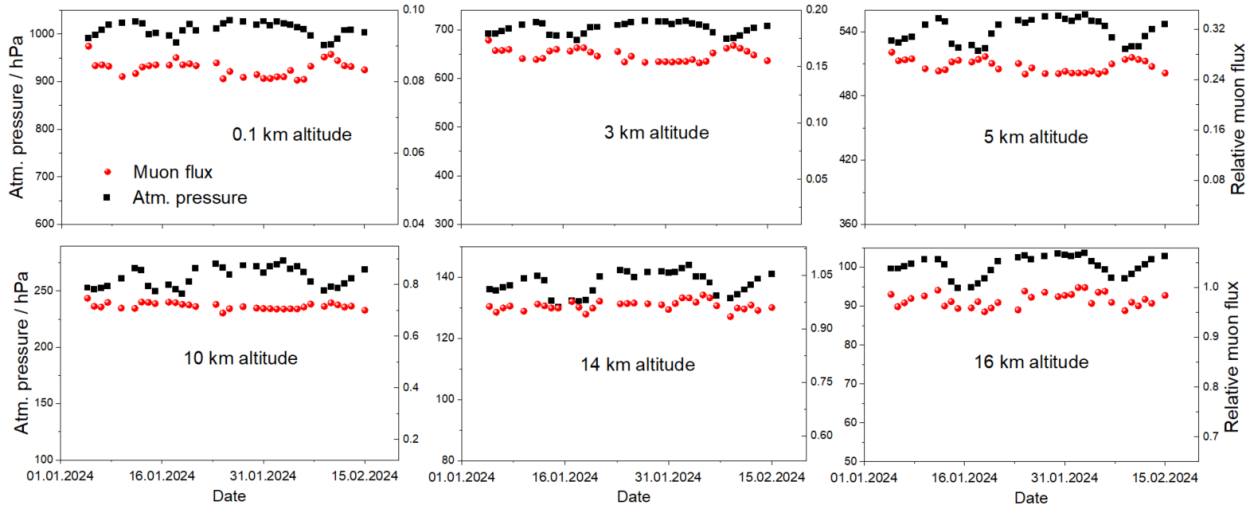

Figure 9: Comparison of simulated muon with atmospheric pressure at different altitudes. Below 10.5 km, the muon flux and pressure exhibit an inverse correlation, whereas above this altitude, they show a positive correlation, meaning the muon flux rate and pressure follow the same temporal trend.

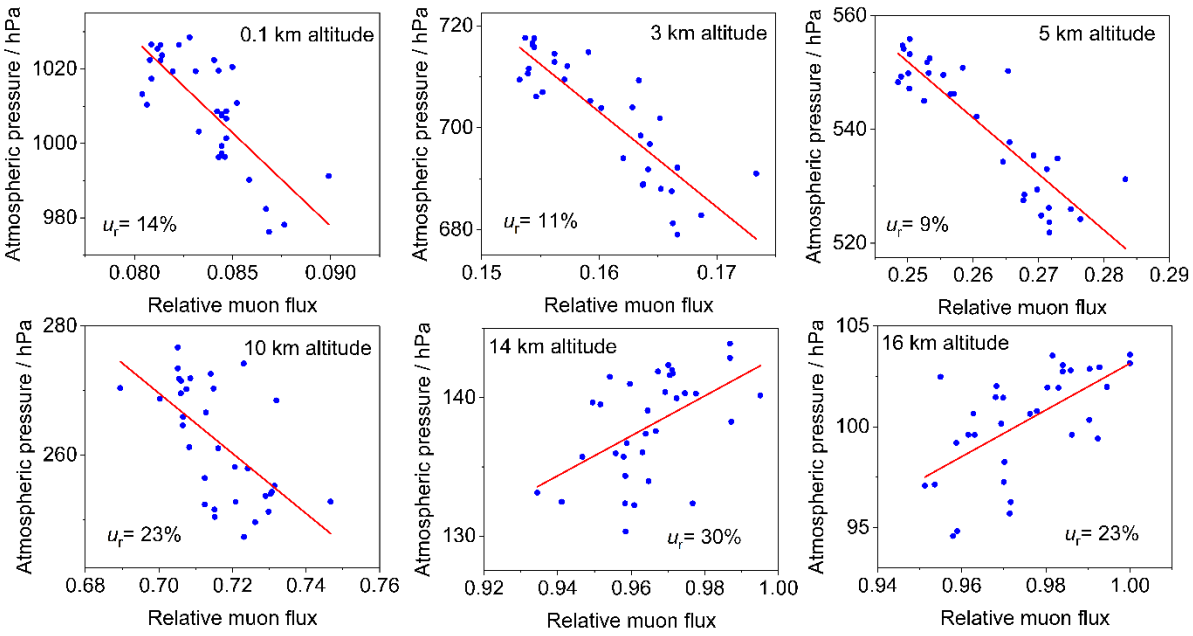

Figure 10: Scatter plots of the relative muon fluxes (I/I_{ref}, with I_{ref}= 0.12836 $cm^{-2}s^{-1}$) shown in Figure 9 as a function of atmospheric pressure. The red lines represent linear fits obtained using ordinary least squares (OLS) regression. The relative uncertainties u_r of the fitted slopes are reported in each panel. At low altitudes (0.1–10 km), the slopes are negative, indicating the expected inverse correlation between muon flux and pressure. However, above ~10.5 km (14 km and 16 km panels), the slopes become positive, reflecting a reversal in the pressure dependence.

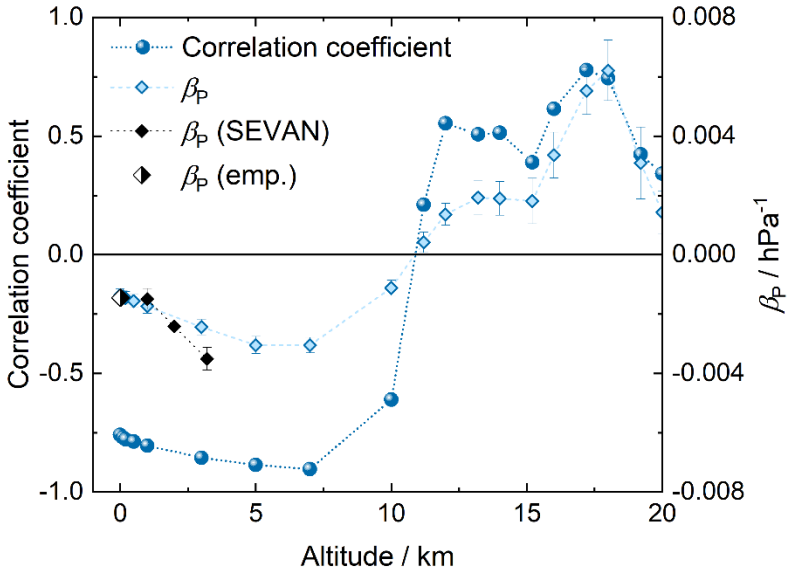

Figure 11: Pearson correlation coefficient between atmospheric pressure and muon flux rate, and barometric coefficient ($\boldsymbol{\beta_P} = (\boldsymbol{\Delta\dot{\phi}}/\dot{\boldsymbol{\phi}})/\boldsymbol{\Delta p}$, with $\dot{\boldsymbol{\phi}}$ being the muon flux rate and $\boldsymbol{\Delta p}$ being the change in atmospheric pressure) as a function of altitude. The values of the barometric coefficient deduced from measurements with SEVAN detectors are shown as black diamonds, while the value predicted by the empirical model of Mendonça et al. (2019) is shown as a half-filled diamond.

This effect is also reflected in the barometric coefficient which is needed to correct the pressure effects in the observed muon data (Al-Qaaod et al., 2025). *Figure **11*** shows also the barometric coefficient as a function of altitude over Brussels. At ground level, the barometric coefficient is determined to be β_P = (- 0.14 ± 0.02) % hPa^{-1}, consistent with the empirical value -0.145 % hPa^{-1} predicted by the empirical curve in Mendonça et al. (2019) for a cutoff rigidity of R_c=3.2 GV (specific to Brussels). The values deduced with SEVAN detectors [Chilingarian and Karapetyan (2011)] at altitudes of 1000 m, 2000 m, and 3200 m are (−0.149±0.035) % hPa^{-1}, (−0.242±0.022) % hPa^{-1}, and (−0.351±0.038) % hPa^{-1}, respectively, and are shown in *Figure **11***. The values at 1000 m and 2000 m compare well with our simulation results of −0.17 % hPa^{-1} and −0.21 % hPa^{-1}, respectively, while at 3200 m the calculated value of -0.25 % hPa^{-1} shows a somewhat larger relative difference (≈28 %). Nevertheless, all experimentally deduced barometric coefficients confirm the same decreasing trend with altitude. Although these data were obtained at higher cutoff rigidity, we show below that cutoff rigidity has no significant influence on the barometric coefficient.

The dependence on the altitude reflects the dependence of muon flux with altitude (see *Figure **5***(a)). The change in the sign of the barometric coefficient near 10.5 km coincides with the altitude of the tropopause in the atmospheric profiles used. Since most muons are produced above this altitude, no significant new contribution to the muon budget occurs below it; instead, muons only undergo increasing energy loss and decay as the overlying atmospheric mass grows with decreasing altitude. Consequently, muon flux decreases as pressure increases, resulting in a

negative correlation. Above 10.5 km, and particularly above the Pfotzer maximum, muon production is substantial because as the atmosphere gets denser with the decreasing altitude, more primary protons interact with it and produce pions, and thus more pions decaying into muons. In this region, muon flux increases with decreasing altitude, same as pressure increases with decreasing altitude, leading to a positive correlation. The vertical temperature and pressure profiles derived from radiosonde data directly determine both the altitude of the tropopause and the atmospheric density gradient, thereby controlling the precise altitude of this sign reversal.

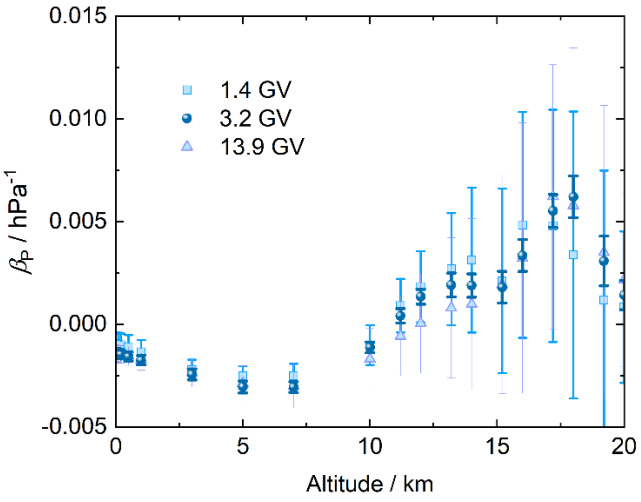

Figure 12: Barometric coefficient, β_P, utilizing atmospheric profiles over Brussels, but with variations in the truncation of the primary cosmic ray spectrum achieved by adjusting the cutoff rigidity.

*Figure **12*** presents the barometric coefficient as a function of altitude for different cutoff rigidities, which account for the truncation of the primary cosmic ray spectrum due to Earth's magnetic field. Each simulation point is derived using the same vertical atmospheric profiles as in *Figure **11***. The objective is to demonstrate the altitude dependence of the barometric coefficient by exclusively varying the cutoff rigidity (i.e., truncating the primary cosmic ray spectrum), without introducing additional atmospheric parameters as degrees of freedom. The barometric coefficient generally exhibits a slight increase with higher cutoff rigidity (R_c) (Mendonça et al., 2019). However, for altitudes below the tropopause, the changes in the barometric coefficient fall within the uncertainties caused by fluctuations in atmospheric parameters. This behavior could be well related to the fact that all simulations employ the same vertical profiles of pressure and temperature.

3 Correlation of PCR with SCR

3.1 Propagation of monoenergetic protons through a standard atmosphere

To correlate PCR with SCR, the relationship between the energy of primary protons and the resulting SCR flux must be established. Specifically, it is necessary to determine the SCR flux at a given altitude h (h=0 corresponds to ground level) produced by a primary proton of energy E_p. This relationship forms the basis for linking primary cosmic ray spectra with observed secondary particle intensities across different atmospheric layers.

Establishing this correspondence requires detailed modeling of the particle cascades initiated by high-energy protons as they traverse the atmosphere. The Monte Carlo simulation framework described in Sect. 2.1 is used to track the production, transport, and attenuation of secondary particles, including muons, neutrons, electrons, electromagnetic components, and other particles. In this case, simulations involve propagating monoenergetic protons through a standard atmosphere rather than a local geographical atmosphere. This provides a consistent reference profile for atmospheric density, composition, and temperature which reflects average atmospheric conditions (minimizing variability due to local weather patterns or seasonal fluctuations).

The standard atmosphere is a static atmospheric model describing how Earth's atmospheric pressure, temperature, density, and viscosity vary with altitude. The model was first issued in 1958 by the U.S. Committee on Extension to the Standard Atmosphere and revised in 1962, 1966, and 1976 (NOAA, 1976). Methodologically it aligns closely with the International Standard Atmosphere (ISA), with the primary differences arising in the prescribed temperature profile at higher altitudes. Key features include:

Simulation approach

In the simulation, a monoenergetic proton with energy E_p is propagated through a rectangular simulation volume with base A=2 km x 2 km and height H=65 km.

The number of particles crossing an area A per unit time is quantified by the fluence rate $\dot{\phi}$,

$$\dot{\phi} = \frac{\dot{N}}{A} \quad [\mathrm{cm}^{-2}\ \mathrm{s}^{-1}], \tag{1}$$

In MCNP, PHITS, and the ICRU (e.g., ICRU Report 60), this quantity is the same as what is commonly termed flux in cosmic-ray physics.

For a source emitting uniformly at $\dot{N}$ = 1 s^{-1} over an area A= 2 km x 2 km=4 x 10^{10} cm^2 the resulting fluence rate is

$$\dot{\phi} = \frac{1}{4 \times 10^{10}\ \mathrm{cm}^2} = 2.5 \times 10^{-11}\ \mathrm{cm}^{-2}\mathrm{s}^{-1}$$

This is extremely low because a single particle per second is distributed over a very large area. In MCNP, tallies are reported per source particle. To model an incident fluence rate of 1 $cm^{-2}s^{-1}$ over the 2 km x 2 km, one can scale the source strength by setting `wgt=4 \times 10^10` in the MCNP6 SDEF (or equivalently multiply tally results by 4×10^{10}). This makes the effective emission rate $\dot{N}$ = 4×10^{10} s^{-1}, yielding $\dot{\phi}$ = 1 $cm^{-2}s^{-1}$ on that plane.

When primary protons propagate through the atmosphere (e.g., standard atmosphere, or a specific atmosphere based on the radiosonde data), secondary particles such as muons, neutrons, electrons, pions, etc., will be generated. Monte Carlo codes such as MCNP or PHITS will output fluxes at different altitudes in particles/(cm^2 source). For each primary proton with energy $E_{\mathrm{p},i}$, the MCNP F2 tally will produce particle fluence spectra $\phi_i(E_{\mathrm{SCR},j}|\, E_{\mathrm{p},i})$, with $E_{\mathrm{SCR},j}$ being the energy of SCR particle, representing the number of SCR particles per cm^2 in the energy bin $j = (E_{\mathrm{SCR},j}, E_{\mathrm{SCR},j+1})$. This particle fluence spectra represents the SCR yield per proton $Y(E_{\mathrm{SCR}}, h|\, E_{\mathrm{p}})$.

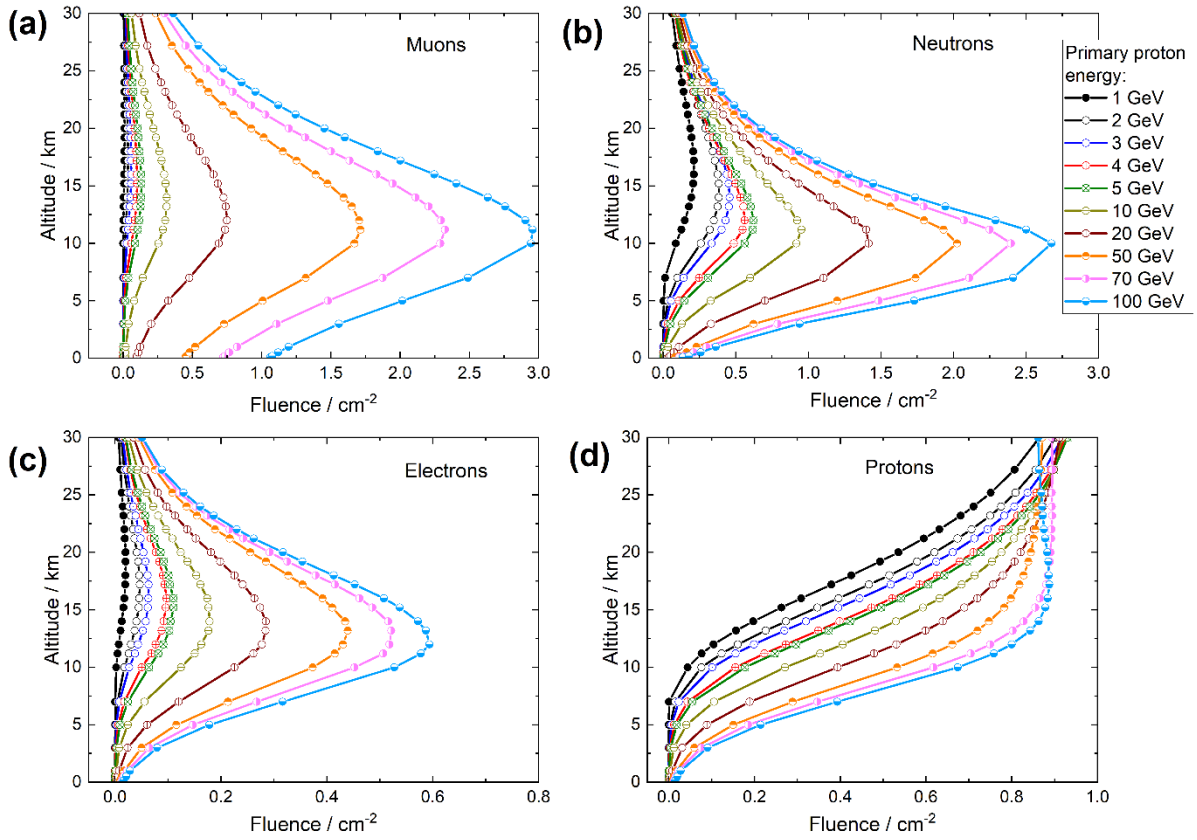

Figure 13: SCR fluxes generated by the propagation of monoenergetic protons with energies of 1 GeV, 2 GeV, 3 GeV, 4 GeV, 5 GeV, 10 GeV, 20 GeV, 50 GeV, 70 GeV, and 100 GeV: (a) muon fluence generated by 1 primary proton per cm², (b) neutron fluence generated by 1 primary proton per cm², (c) electron fluence generated by 1 primary proton per cm², and (d) proton fluence generated by 1 primary proton per cm².

Figure 13 shows the fluences of SCR particles, integrated over SCR particle energy ($\sum_{\mathrm{j}}\, \phi_{\mathrm{i}}(E_{\mathrm{SCR,j}}|\, E_{\mathrm{p,i}})$), generated by a monoenergetic proton source of 1 proton/(cm^2·s) propagating through a standard atmosphere. Panels (a) to (c) illustrate that secondary particles produced in the atmosphere, such as muons, neutrons, and electrons, exhibit a pronounced maximum in flux

between approximately 10 km and 15 km altitude. This feature corresponds to the Pfotzer maximum described in Section 2.2.2.

Above this maximum, the atmospheric depth is insufficient for the particle cascade to fully develop, so the number of secondary particles continues to increase with depth. At the maximum itself, the production rate of secondaries per unit atmospheric depth reaches its peak. Below this altitude, absorption and decay processes dominate over new production, leading to a decline in flux.

The figure also shows that as the energy of the primary protons increases, the maximum SCR flux becomes larger and shifts progressively toward lower altitudes. In contrast, the altitude profile of protons, shown in panel (d), does not exhibit such behavior. Instead, proton flux decreases monotonically with increasing atmospheric depth. At high altitudes, primary protons are still abundant, but as they penetrate deeper into the atmosphere, they are absorbed or undergo fragmentation. Unlike mesons and leptons, there is no significant replenishment of protons via decay, so no maximum is formed.

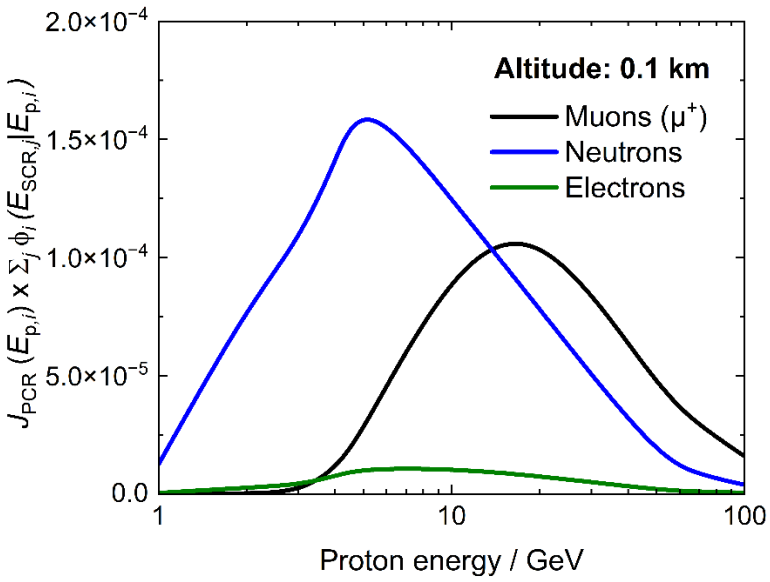

Figure 14: Fluence of neutrons, muons, and electrons at an altitude of 100 m as a function of primary proton energy, obtained from the MCNP6-based atmospheric model. Units of J_{PCR} and ϕ_i are $cm^{-2}\ s^{-1}\ sr^{-1}\ GeV^{-1}$ and cm^{-2}, respectively.

Figure 14 shows the fluence of neutrons, muons, and electrons at an altitude of 100 m as a function of the primary proton energy, obtained with the MCNP6-based atmospheric model. The results indicate that ground-level neutrons are predominantly produced by lower-energy primaries compared to muons. This explains why Forbush decreases (FDs) are generally larger in neutron monitor data than in muon measurements. Muons observed at the surface originate mainly from primaries above a few GeV, which are only weakly influenced by heliospheric magnetic field disturbances. Neutrons, on the other hand, receive significant contributions from lower-energy primaries that are more strongly modulated, leading to a deeper FD signature.

3.2 SCR fluence on the ground

The fluence spectra of secondary cosmic radiation observed at ground level cannot be attributed to the interaction of few monoenergetic primary protons alone. In reality, the secondary particle field is the result of the entire primary cosmic ray spectrum, which spans many orders of magnitude in energy and includes not only protons but also heavier nuclei. Each component of this spectrum contributes differently to the development of atmospheric cascades: lower-energy primaries are largely absorbed before reaching the ground, while higher-energy primaries initiate extensive air showers that penetrate to sea level. Consequently, the SCR fluence spectra measured on the ground, $\Phi(E_{\mathrm{SCR}})$, are the integral response to the full primary cosmic-ray spectrum and composition, folded with the energy- and species-dependent SCR yields.

In the following, the analysis is restricted to ground-level muons, with protons taken as the sole primary component. Muons are the most abundant charged secondaries at sea level, with long lifetimes and high penetration depth, making them the dominant contributor to ground-level cosmic radiation and one of the key observable in cosmic-ray monitoring. Restricting the primaries to protons is a common and reasonable approximation, since they constitute about 85–90% of the galactic cosmic-ray flux. While heavier nuclei and other species do contribute to secondary production, their effects can often be represented to first order by scaling proton-induced cascades. This simplification allows us to isolate the essential features of cascade development while maintaining computational feasibility.

The number of primary protons impinging on the area *dA* in a time *dt* with energies in the range between E_{p} and $E_{\mathrm{p}}+dE_{\mathrm{p}}$ is

(2) $$dN_{\mathrm{p}} = J_{\mathrm{p}}(E_{\mathrm{p}},\Omega_{\mathrm{p}}) \underbrace{\cos\theta_{\mathrm{p}}}_{\text{projected area}} d\Omega_{\mathrm{p}}\, dE_{\mathrm{p}}\, dA\, dt$$

with $J_{\mathrm{p}}(E_{\mathrm{p}},\Omega_{\mathrm{p}})$ being the proton differential intensity in $\mathrm{cm^{-2}s^{-1}sr^{-1}GeV^{-1}}$ at the top of atmosphere (TOA) and θ_{p} being the zenith angle of primary protons.

dN_{p} primary particles contribute to the ground-level muon fluence by

(3) $$Y(E_{\mu},h|\,E_{\mathrm{p}},\Omega_{\mathrm{p}}) \times \frac{dN_{\mathrm{p}}}{dA\,dt}$$

The yield $Y(E_{\mu},h|\,E_{\mathrm{p}},\Omega_{\mathrm{p}})$ generated by F2 is per unit detector area, while the physical primary spectrum $J_{\mathrm{p}}(E_{\mathrm{p}},\Omega_{\mathrm{p}})$ is per unit TOA area. For primary protons sampled uniformly over the top horizontal cross-section of the simulated volume, the effective injection area per source is

$$A_{\mathrm{s}} = (2\ \mathrm{km}) \times (2\ \mathrm{km})$$

One MCNP "source history" in our setup represents one primary chosen uniformly over the injection region A_{s}. Multiplying $J_{\mathrm{p}}(E_{\mathrm{p}},\Omega_{\mathrm{p}})$ with A_{s}, we get the number of primaries per second, per solid angle, per energy bin dE_{p} emitted by the source area A_{s},

(4) $$A_{\mathrm{s}} \cdot J_{\mathrm{p}}(E_{\mathrm{p}},\Omega_{\mathrm{p}}) \longrightarrow \frac{number\ of\ protons\ emitted\ by\ area\ A_{\mathrm{s}}\ of\ the\ source}{dt\ d\Omega_{\mathrm{p}}\ dE_{\mathrm{p}}} \quad [\mathrm{s^{-1}\ sr^{-1}\ GeV^{-1}}]$$

Substituting (2) into (3), and using (4) we get for the muon fluence rate on the ground due to dN_{p} primary protons

(5) $$Y(E_\mu, h|E_p, \Omega_p)\ A_s\ J_p(E_p, \Omega_p)\ \cos\theta_p\ d\Omega_p\ dE_p$$

Integrating over all primaries (energy and directions) that arrive from the downward hemisphere we get the muon fluence rate at the altitude *h*, $\Phi_\mu(E_\mu, h)$, due to the primary differential energy spectrum $J_p(E_p, \Omega_p)$,

(6) $$\Phi_\mu(E_\mu, h) = \int dE_p \int_{down} d\Omega_p\ A_s\, J_p(E_p, \Omega_p)\ \cos\theta_p\ Y(E_\mu, h|E_p, \Omega_p)$$

If we make two common approximations:

i. Downward isotropic primaries: $J_p(E_p, \Omega_p) = J_p(E_p)$ (no directional dependence).

ii. Use vertical-primary yields as a proxy for all Ω_p: $Y(E_\mu, h|E_p, \Omega_p) \approx Y(E_\mu, h|E_p)$.

Then the angular integral is just

(7) $$\int_{hemisphere} \cos\theta_p\, d\Omega_p = \int_0^{2\pi} \int_0^{\pi/2} cos\ \theta\ \ sin\ \theta\ \ d\theta\ = 2\pi\ \cdot \frac{1}{2} = \pi\,.$$

So (6) reduces to:

(8) $$\Phi_\mu(E_\mu, h)\ \approx\ \pi \int dE_p\ \ A_s\, J_p(E_p)\, Y(E_\mu, h|E_p)$$

With a discrete primary grid $\{E_{p,i}\}$ and bin widths w_i (linear: ΔE_i, or log-midpoint: $E_{p,i}\Delta \ln E_i$):

(9) $$\Phi_\mu(E_\mu, h)\ \approx\ \pi\, A_s \sum_i Y(\,E_\mu, h \mid E_{p,i}\,)\ \ J_p(E_{p,i})\ \ w_i$$

This equation represents the muon fluence rate in $cm^{-2}s^{-1}$ at an altitude *h* assuming downward isotropic primaries. By knowing the proton yield $Y(\,E_\mu, h \mid E_{p,i}\,)$ at the altitude h (see Figure 13), and primary spectrum $J_p(E_p, \Omega_p)$ one can compute the muon fluence rate at that altitude $\Phi_\mu(E_\mu)$.

Energy binning for $E_{p,i}$

Since cosmic-ray primaries follow a steep power law (~$E^{-2.7}$), it's best to treat the sparse grid in log-energy. One option is to make Voronoi bins in log *E* around each simulated primary energy, i.e., use geometric midpoints as bin edges.

Given simulated $E_{p,i} = \{1, 2, 3, 4, 5, 10, 20, 50, 70, 100\}$ GeV, we have

Internal bin edges:

(10) $$E_{i-\frac{1}{2}} = \sqrt{E_{p,i} \cdot E_{p,i-1}} \quad ; \quad E_{i+\frac{1}{2}} = \sqrt{E_{p,i} \cdot E_{p,i+1}}$$

First edge:

(11) $$E_{1-\frac{1}{2}} = \frac{E_{\mathrm{p},1}^2}{E_{\mathrm{p}.2}}$$

Last edge:

(12) $$E_{N+\frac{1}{2}} = \frac{E_{\mathrm{p,N}}^2}{E_{\mathrm{p,N}-1}}$$

The bin widths w_i can be computed using two approaches, logarithmic and linear. The log-bin width is equivalent to integrating in the variable $\ln E$ (since $dE = E\, d\,(\ln E)$) and is more stable for power-law spectra than linear widths $E_{i+1/2} - E_{i-1/2}$. For linear bins, expect larger discretization error at high energies where your bins are wider in linear space.

The **log-bin widths w_i are**

$$w_i^{(\log)} = \int_{E_{i-\frac{1}{2}}}^{E_{i+\frac{1}{2}}} dE = \int_{E_{i-\frac{1}{2}}}^{E_{i+\frac{1}{2}}} E\, d\,(\ln E) \approx \int_{E_{i-\frac{1}{2}}}^{E_{i+\frac{1}{2}}} E_{p,i}\, d\,(\ln E) = E_{p,i} \int_{E_{i-\frac{1}{2}}}^{E_{i+\frac{1}{2}}} d\,(\ln E)$$

(13) $$= E_{p,i}\left[\ln\left(E_{i+\frac{1}{2}}\right) - \ln\left(E_{i-\frac{1}{2}}\right)\right] = E_{p,i} \ln\left(\frac{E_{i+\frac{1}{2}}}{E_{i-\frac{1}{2}}}\right)$$

while for the linear ones we have

(14) $$w_i^{(\mathrm{lin})} = \int_{E_{i-\frac{1}{2}}}^{E_{i+\frac{1}{2}}} dE = E_{i+\frac{1}{2}} - E_{i-\frac{1}{2}}$$

3.3 Primary differential energy spectrum

Cosmic rays arriving at Earth span a wide range of energies, and their distribution is typically described by the differential energy spectrum, $J(E)$, which gives the flux of particles per unit energy interval, per unit area, per unit solid angle, and per unit time (typically in $m^{-2}\ s^{-1}\ sr^{-1}\ GeV^{-1}$). Over much of the energy range relevant for space and atmospheric radiation studies, this spectrum follows an approximate power law, $J(E) \propto E^{-\gamma}$, with $\gamma \approx 2.7$ (Grieder, 2001). However, the spectrum measured near Earth is not the same as the spectrum in interstellar space. Before reaching the top of the atmosphere, galactic cosmic rays (GCRs) must traverse the heliosphere, where they experience diffusion, convection, adiabatic energy losses, and drift effects due to the solar wind and the interplanetary magnetic field.

A widely used framework to account for these solar modulation effects is the force-field approximation (FFA) (Gleeson and Axford, 1968; Usoskin et al., 2005). In this model, the complex processes of transport in the heliosphere are reduced to a single effective parameter, the modulation

potential ϕ (typically given in GV), see Eq.(15); The local interstellar spectrum (LIS), $J_{\mathrm{LIS}}(T)$, is shifted in energy and scaled in intensity to yield the modulated spectrum at 1 AU,

$$J(T) = A_{\mathrm{FFA}}(T, \Phi) \cdot J_{\mathrm{LIS}}(T + \Phi) \tag{15}$$

with

$$A_{\mathrm{FFA}}(T, \Phi) = \frac{(T + m_0c^2)^2 - (m_0c^2)^2}{(T + \Phi + m_0c^2)^2 - (m_0c^2)^2} \tag{16}$$

where:

- $J(T)$: differential intensity (or differential primary flux spectra) at Earth,
- *T:* is the kinetic energy (in GeV per nucleon) of the primary particle,
- $\Phi = (Ze/A)\phi$: is the kinetic energy-shift due to the modulation potential ϕ,
- ϕ: modulation potential,
- $J_{\mathrm{LIS}}(T + \Phi)$: local interstellar spectrum (i.e., primary differential flux) at a shifted energy,
- m_0: rest mass of the primary particle,
- *Z*: charge number of the primary particle,
- *A*: mass number of the primary particle
- *e*: elementary charge of the primary particle.

The LIS spectrum can be computed using the formula given by Usoskin et al. (2005):

$$J_{LIS-Usoskin}(T) = \frac{1 \times 10^9 \times [P(T)]^{-2.78}}{1 + 0.4866 \times [P(T)]^{-2.51}} \tag{17}$$

with

$$P(T) = \sqrt{T\,(T + 2\,m_0c^2)} \tag{18}$$

Each cosmic ray particle appears to lose an average energy of $\Phi = (Ze/A)\phi$ when entering the heliosphere. The magnitude of J_{LIS} is reduced by an amplitude factor $A_{\mathrm{FFA}}(T, \Phi)$, see Figure 15. From this figure it is evident that the heliosphere modulation potential affects mainly low energy protons. It suppresses the differential energy spectrum at low energies (T<10 GeV) significantly, see Figure 16. At kinetic energies above 10 GeV the influence of ϕ diminishes rapidly and $A_{\mathrm{FFA}}(T, \Phi)$ converges to zero at about 100 GeV.

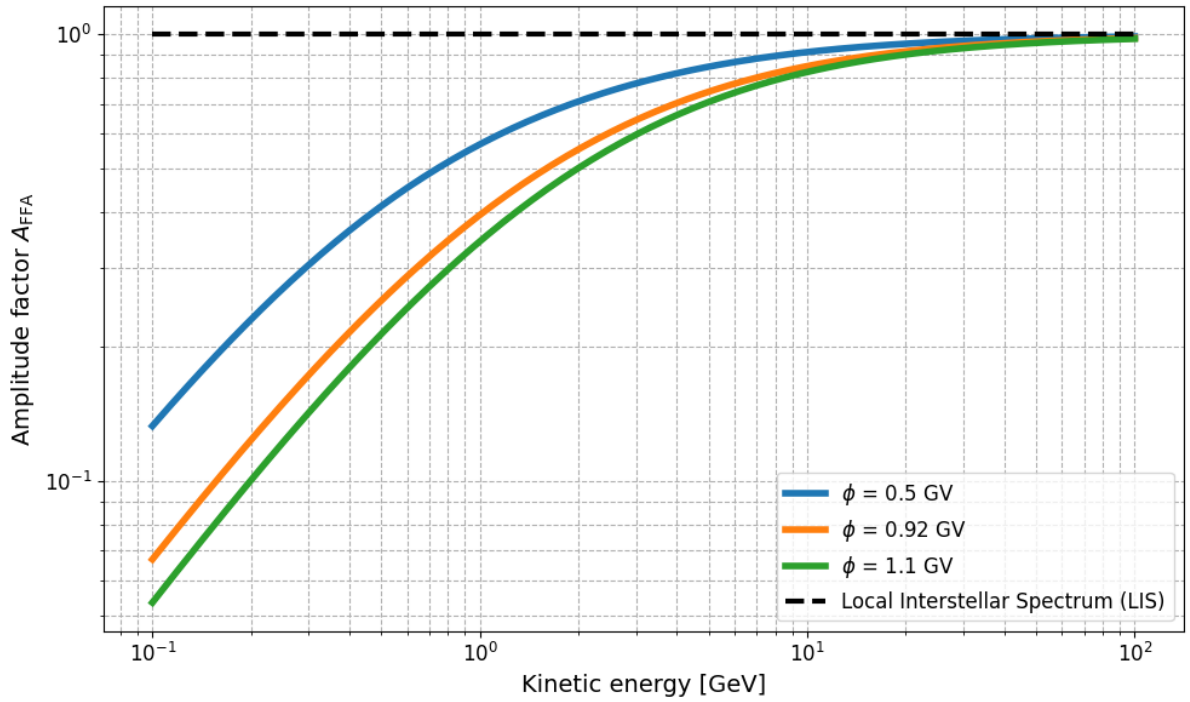

Figure 15: The FFA amplitude factor $A_{FFA}(T,\Phi)$.

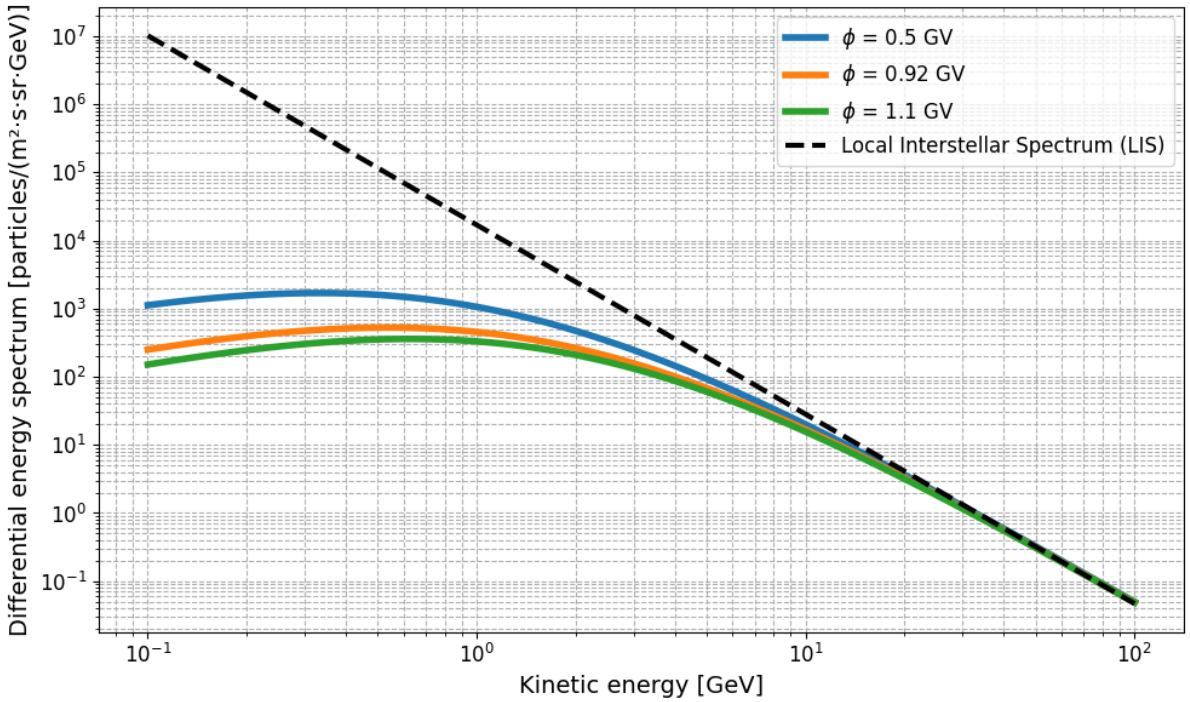

Figure 16: Differential energy spectra of primary cosmic rays at Earth computed using Eq. (15).

3.4 Deducing J_{PCR} from J_{SCR}: parametric forward fitting of the primary spectrum

When we want to deduce the spectrum of primary protons arriving at the top of the atmosphere from measurements of secondary muons at ground level, we face an inverse problem. The measured muon flux $\Phi_\mu(\mathrm{E}_\mu, h)$ is related to the unknown primary proton spectrum J through the muon yield function Y [see Eq. (9)]:

$$\Phi_j = \sum_i Y_{ji}\, J_i\, w_i, \tag{19}$$

where j labels muon energy bins, i labels primary proton energy bins, and w_i is the bin width in primary energy. Directly inverting this relationship is not stable: the response matrix is ill-conditioned and small measurement uncertainties lead to large unphysical oscillations in the reconstructed spectrum.

Direct inversion can be avoided by forward fitting a parametric model of the proton spectrum.

Step 1: **Choose a functional form for the primary spectrum**

Instead of solving for each bin J_i independently, we assume that the spectrum follows a simple, smooth law with a few free parameters. Typical choices are:

Power law:

$$J(E_\mathrm{p}) = J_0\, E_\mathrm{p}^{-\gamma} \tag{20}$$

Power law with exponential rollover (useful for solar particle events):

$$J(E_\mathrm{p}) = J_0\, E_\mathrm{p}^{-\gamma}\, e^{-E_\mathrm{p}/E_0} \tag{21}$$

Such forms are well justified, since the spectra of cosmic rays and solar particles often closely resemble power laws.

Step 2: Compute the expected muon flux

For a given set of parameters $\theta = (J_0, \gamma, E_0, \dots)$, we calculate the predicted muon spectrum by folding the assumed proton spectrum with the yield function:

$$\widehat{\Phi}_j(\theta) = \sum_i Y_{ji}\, J(E_{p,i}; \theta)\, w_i. \tag{22}$$

This step is called forward folding: we predict what the detector should see, given a trial primary spectrum.

Step 3: Define a goodness-of-fit function

We compare the predicted muon flux $\widehat{\Phi}_i(\theta)$with the measured flux Φ_i. If the measurement errors are approximately Gaussian with standard deviations σ_i, we use the chi-squared statistic:

$$\chi^2(\theta) = \sum_j \left[\frac{\Phi_j - \widehat{\Phi}_j(\theta)}{\sigma_j}\right]^2. \quad (23)$$

Step 4: Minimize to obtain best-fit parameters

The best estimate of the proton spectrum parameters $\hat{\theta}$ is obtained by minimizing $\chi^2(\theta)$.

3.5 Matrix formulation of the differential SCR flux

Let us consider Eq. (9): When PCR-related quantities are labeled with the index *i* (e.g., proton energies E_p with $E_{p,i}$ = 0.5 GeV, 1, GeV, 2 GeV,…, 500 GeV), and SCR-related quantities are labeled with the index *j* (e.g., muon energies E_μ with $E_{\mu,j}$= 0.1 MeV, 1 MeV, 10 MeV, 1 GeV, …,10 GeV), this equation can be written as:

$$\begin{aligned}\Phi_\mu(E_{\mu,1}) &= \pi A_s \{Y(E_{\mu,1} \mid E_{p,1})\ J_p(E_{p,1})\ w_1 \\ &+ Y(E_{\mu,1} \mid E_{p,2})\ J_p(E_{p,2})\ w_2 \\ &+ Y(E_{\mu,1} \mid E_{p,3})\ J_p(E_{p,3})\ w_3 \\ &+ Y(E_{\mu,1} \mid E_{p,4})\ J_p(E_{p,4})\ w_4 \\ &+ \cdots \\ &+ Y(E_{\mu,1} \mid E_{p,n})\ J_p(E_{p,n})\ w_n\end{aligned} \quad (24)$$

Similar equations to (24) we will have for other SCR energies $E_{\mu,j}$, *j*=2, 3,…, *m*. Thus, equation (9) can be written in a matrix form as

$$\mathbf{J}_{SCR} = \pi A_s \mathbf{Y} \cdot \mathbf{J}_{PCR} \quad (25)$$

with

$$\mathbf{J}_{SCR} = \begin{bmatrix}\Phi_\mu(E_{\mu,1}) \\ \Phi_\mu(E_{\mu,2}) \\ \vdots \\ \Phi_\mu(E_{\mu,m})\end{bmatrix} \quad (26)$$

and

$$\mathbf{Y} = \begin{bmatrix} Y_{11} & Y_{12} & \cdots & Y_{1n} \\ Y_{21} & Y_{22} & \cdots & Y_{2n} \\ \vdots & \vdots & \cdots & \vdots \\ Y_{m1} & Y_{m2} & \cdots & Y_{mn}\end{bmatrix} \quad (27)$$

and

(28) $$\mathbf{J}_{\mathrm{PCR}} = \begin{bmatrix} J_1\, w_1 \\ J_2\, w_2 \\ \vdots \\ J_n\, w_n \end{bmatrix}$$

3.6 Deducing J_{PCR} from J_{SCR}: The matrix method

We start from the system in Eq. (25):

(29) $$\mathbf{J}_{\mathrm{SCR}} = \pi\, A_s\, \mathbf{Y} \cdot \mathbf{J}_{\mathrm{PCR}}$$

with $\mathbf{J}_{\mathrm{SCR}}$ of size *m*×1, $\mathbf{Y}$ of size *m*×*n*, and $\mathbf{J}_{\mathrm{PCR}}$of size *n*×1.

Y cannot be inverted because it is not square (typically, *m*>*n*.) A non-square matrix doesn't have an ordinary inverse. But we can still look for a J_{SCR} that makes the equation as close as possible (least-squares).

The least-squares approach

We want $\mathbf{J}_{\mathrm{PCR}}$ such that

(30) $$\mathbf{Y} \cdot \mathbf{J}_{\mathrm{PCR}} \approx \frac{1}{\pi\, A_{\mathrm{s}}}\, \mathbf{J}_{\mathrm{SCR}}$$

is as close as possible. So we minimize the error (residual):

(31) $$\mathbf{R}(\mathbf{J}_{\mathrm{PCR}}) = \left| \mathbf{Y} \cdot \mathbf{J}_{\mathrm{PCR}} - \frac{1}{\pi\, A_{\mathrm{s}}}\, \mathbf{J}_{\mathrm{SCR}} \right|^2$$

By taking the the derivative of $\mathbf{R}(\mathbf{J}_{\boldsymbol{PCR}})$ with respect to $\mathbf{J}_{\mathrm{PCR}}$ and set it to zero:

(32) $$\frac{\partial \mathbf{R}(\mathbf{J}_{\mathrm{PCR}})}{\partial \mathbf{J}_{\mathrm{PCR}}} = 2\, \mathbf{Y}^{\mathbf{T}} \cdot \left(\mathbf{Y} \cdot \mathbf{J}_{\mathrm{PCR}} - \frac{1}{\pi\, A_{\mathrm{s}}}\, \mathbf{J}_{\mathrm{SCR}} \right) = 2 \left(\mathbf{Y}^{\mathbf{T}} \cdot \mathbf{Y} \cdot \mathbf{J}_{\mathrm{PCR}} - \frac{1}{\pi\, A_{\mathrm{s}}}\, \mathbf{Y}^{\mathbf{T}} \cdot \mathbf{J}_{\mathrm{SCR}} \right) = \mathbf{0}$$

With $\mathbf{Y}^{\mathbf{T}}$ being the transpose of matrix $\mathbf{Y}$.

Rearranging

From Eq. (32) we obtain matrix equation:

(33) $$\mathbf{Y}^{\mathbf{T}} \cdot \mathbf{Y} \cdot \mathbf{J}_{\mathrm{PCR}} = \frac{1}{\pi\, A_{\mathrm{s}}}\, \mathbf{Y}^{\mathbf{T}} \cdot \mathbf{J}_{\mathrm{SCR}}$$

Solve for $\mathbf{J}_{\mathrm{PCR}}$

If $\mathbf{Y}$ has full column rank, then $\mathbf{Y}^{\mathbf{T}} \cdot \mathbf{Y}$ is square (*n*×*n*) and invertible:

(34) $$\mathbf{J}_{\mathrm{PCR}} = \frac{1}{\pi A_{\mathrm{s}}} \left(\mathbf{Y}^{\mathbf{T}} \cdot \mathbf{Y}\right)^{-1} \cdot \mathbf{Y}^{\mathbf{T}} \cdot \mathbf{J}_{\mathrm{SCR}}$$

That's the least-squares solution. Here the transpose $\mathbf{Y}^{\mathbf{T}}$naturally appears when we minimize the squared error — not because we "guessed" it, but because it comes directly from the calculus.

This method is applicable only when a sufficient number of samples at $E_{\mathrm{p},i}$ are available and the sampling frequency is adequate.

3.7 Validation of the methodology: comparison with other MC simulation codes and experimental data

The methodology for correlating secondary cosmic radiation (SCR) with primary cosmic rays (PCR) has been validated through both simulation and observation. First, comparisons were made with results from the EXPACS model, which provides established reference values for SCR fluxes in the troposphere. In addition, the approach was benchmarked against experimental data collected during periods of geomagnetic storms, as observed within the timeline of the BIOSPHERE project and its associated measurement campaigns. These validation steps ensure that the model captures both the expected background behavior of SCR in the atmosphere and its variability in response to solar and geomagnetic disturbances. This dual comparison—against a well-tested simulation tool and real-world measurements—provides confidence in the reliability of the methodology and its applicability to studying cosmic-ray induced radiation at ground and aviation altitudes.

3.7.1 Comparison with EXPACS

EXPACS (EXcel-based Program for calculating Atmospheric Cosmic-ray Spectrum) is a widely used code for estimating cosmic-ray induced particle spectra and dose rates at different altitudes, geomagnetic cut-off rigidities, and solar modulation conditions (Sato, 2015, 2016). T EXPACS was developed at JAEA (Japan Atomic Energy Agency) and is based on pre-calculated Monte Carlo simulations of cosmic-ray transport in the atmosphere using the PHITS (Particle and Heavy Ion Transport code System). The underlying PHITS calculations and resulting datasets have been compared with measured cosmic-ray spectra, neutron fluxes, and dose rates at aircraft altitudes and ground level. Published studies show good agreement with experimental measurements, especially for aviation radiation dosimetry and atmospheric neutron spectrum estimation. EXPACS results are benchmarked against ICRP and ICRU reference data.

Figure 17 and Figure 18 compare the simulated muon fluence rates at altitudes of 100 m and 7000 m for a geomagnetic cutoff rigidity of 2.89 GV. The simulations were performed using the methodology described in Sect. 3.2, with fluences calculated using (9) and primary proton yields as defined in Sect. 3.1. For the local interstellar spectrum (LIS), Eq. (15) was applied with a modulation potential of 0.6 GV. The EXPACS fluence $\Phi[\mathrm{cm}^{-2}\ \mathrm{s}^{-1}]$ was derived from the differential flux in $[\mathrm{cm}^{-2}\ \mathrm{s}^{-1}\ \mathrm{MeV}^{-1}]$ by integrating over the corresponding energy bins.

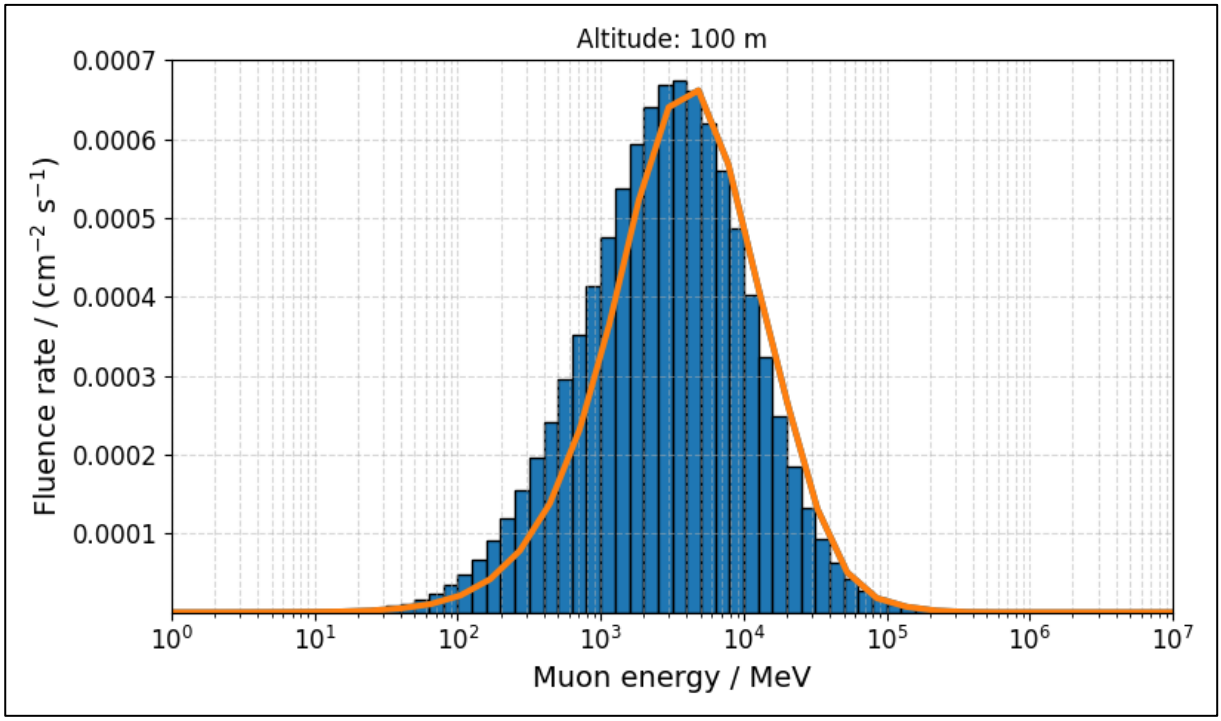

Figure 17: Comparison between the fluence rate obtained from Eq. (9) and EXPACS at an altitude of 100 m and a geomagnetic cutoff rigidity of 2.89 GV.

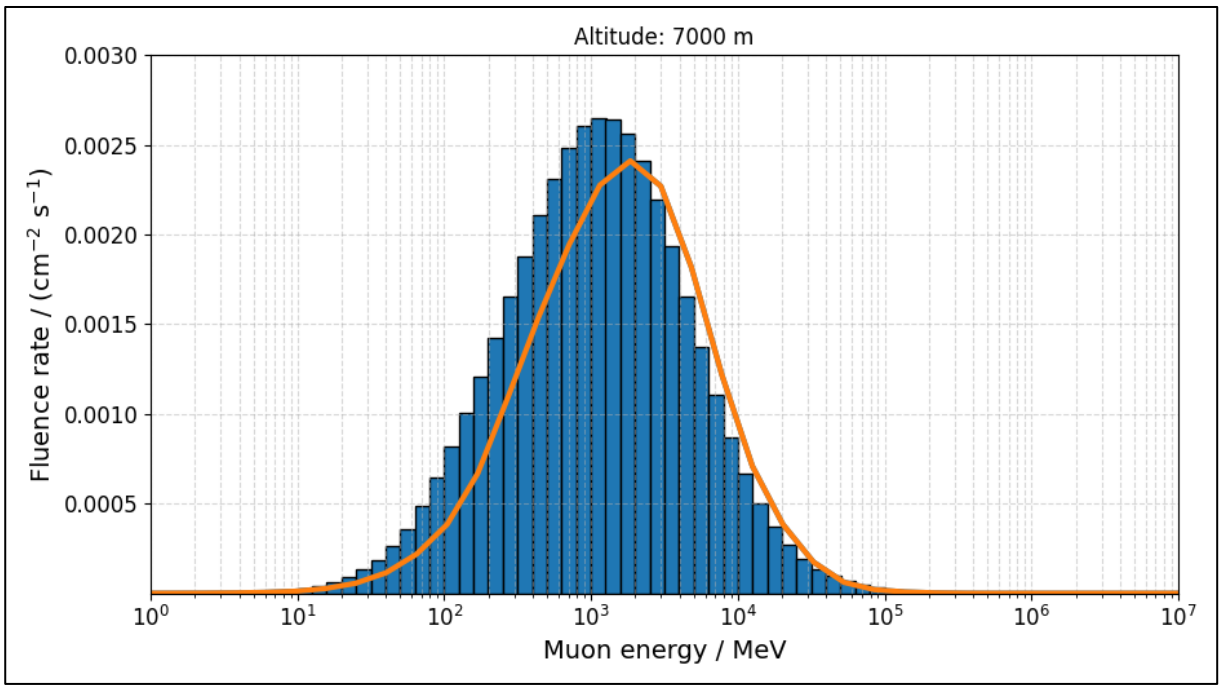

Figure 18: Comparison between the fluence rate obtained from Eq. (9) and EXPACS at an altitude of 7000 m and a geomagnetic cutoff rigidity of 2.89 GV.

Using the provided analysis, we compared the EXPACS and MCNP muon fluence rate spectra at 100 m over the full energy range sampled by each code. The total (energy-integrated) flux predicted by the methodology described in this work, about 15.8 $cm^{-2}s^{-1}$ at 100 m and 31.6 $cm^{-2}\,s^{-1}$ at 7000 m, compares well with the values of EXPACS of 14.5 $cm^{-2}\,s^{-1}$ and 30.9 $cm^{-2}\,s^{-1}$, respectively; These values are only about 2 % to 9% higher than the EXPACS values, indicating strong agreement in overall normalization. A pointwise comparison on the MCNP grid (with EXPACS linearly interpolated to that grid) yields a normalized mean absolute error ($NMAE = \sum_i |\Phi_{\mathrm{MCNP},i} - \Phi_{\mathrm{EXPACS},i}| / \sum_i \Phi_{\mathrm{EXPACS},i}$) of 0.16 to 0.21, and a Spectral Similarity Index [$SSI = \sum_i (\Phi_{\mathrm{MCNP},i} \cdot \Phi_{\mathrm{EXPACS},i}) / \left(\sqrt{\sum_i \Phi^2_{\mathrm{MCNP},i}} \sqrt{\sum_i \Phi^2_{\mathrm{EXPACS},i}}\right)$] of 0.98, demonstrating that the spectral shapes are highly consistent while local deviations remain modest. The MCNP/EXPACS ratio indicates that MCNP tends to underpredict EXPACS at portions of the spectrum on a pointwise basis; however, the overlay and ratio plots show this deficit is energy dependent—agreement tightens markedly toward the GeV region (ratio approaching unity) and can slightly exceed EXPACS in the 10 GeV to 100 GeV band—so that the integrated fluence remains in close accord despite sub-range variations. These results support the conclusion that, for applications driven by total fluence or by spectral shape rather than strict bin-by-bin equality, MCNP and EXPACS provide broadly consistent predictions.

Both figures capture correctly the progressive shift in the peak of the muon distribution, from approximately 1.8 GeV at 7000 m to around 4 GeV at an altitude of 100 m. This shift is accompanied by a significant decrease in muon flux. While muons lose energy as they traverse the atmosphere, the flux at lower altitudes is dominated by higher-energy muons, which are less likely to decay due to time dilation effects, allowing them to penetrate deeper into the atmosphere. In contrast, lower-energy muons are more likely to decay before reaching these altitudes, contributing to the observed upward shift at higher altitudes.

3.7.2 Comparison with Forbush decrease measurements

A Forbush decrease (FD) is a short-term suppression of galactic cosmic ray (GCR) intensity at Earth, typically lasting from several hours to a few days, followed by a gradual recovery phase. It is caused by interplanetary disturbances—often coronal mass ejections (CMEs) and their associated shocks—that enhance the interplanetary magnetic field (IMF) and turbulence, effectively shielding Earth from incoming cosmic rays. In the framework of cosmic ray transport, such a transient shielding effect can be described as a sudden increase in the **modulation potential**, which parameterizes the integrated impact of solar and heliospheric conditions on cosmic ray propagation. A higher modulation potential corresponds to stronger suppression of GCRs, and during a Forbush decrease this manifest as a temporary “step-like” rise in modulation potential superimposed on the longer-term solar modulation trend. In ground-based muon detectors such as DECOS1, which records the secondary muon flux generated by cosmic rays in the atmosphere, this results in a measurable reduction of count rates that can be directly compared with the simulated response under varying modulation conditions.

*Figure **19*** shows the FD measured during the Mother's Day Solar Storm in May 11, 2024 with the PTBs muon detector DECOS1. The figure also compares these observations with the simulated FDs obtained using the methodology developed in this work (Sect. 3.2 to 3.4). To correlate PCR with SCR, we follow the approach described in Sect. 3.4, where analytical functions are applied to link the primary cosmic-ray (PCR) flux with the secondary cosmic radiation (SCR) observed at ground level. In this case, however, instead of deriving J_{PCR} directly from the measured muon data, we use the modulation potential deduced from observations to generate a PCR flux via Eq. (15). This flux is then inserted into Eq. (9) to simulate the expected muon flux at ground level. In this figure, the ϕ-data from stations in OULU, TERA (Terre Adelie, Antarctica / France) and ROME, see *Figure **20***.

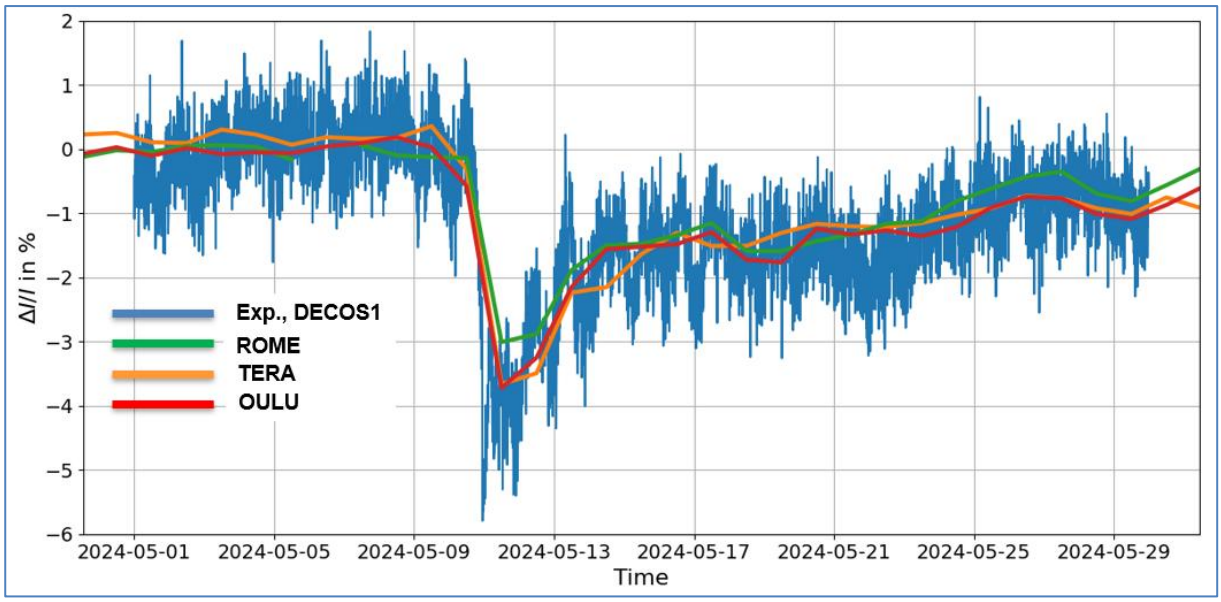

Figure 19: Forbush decrease during the Mother's Day Solar Storm in May 2024. Comparison of ground-based observations with DECOS1 and simulations based on the methodology presented in this work, using modulation potential values derived from OULU, TERA, and ROME neutron monitor data.

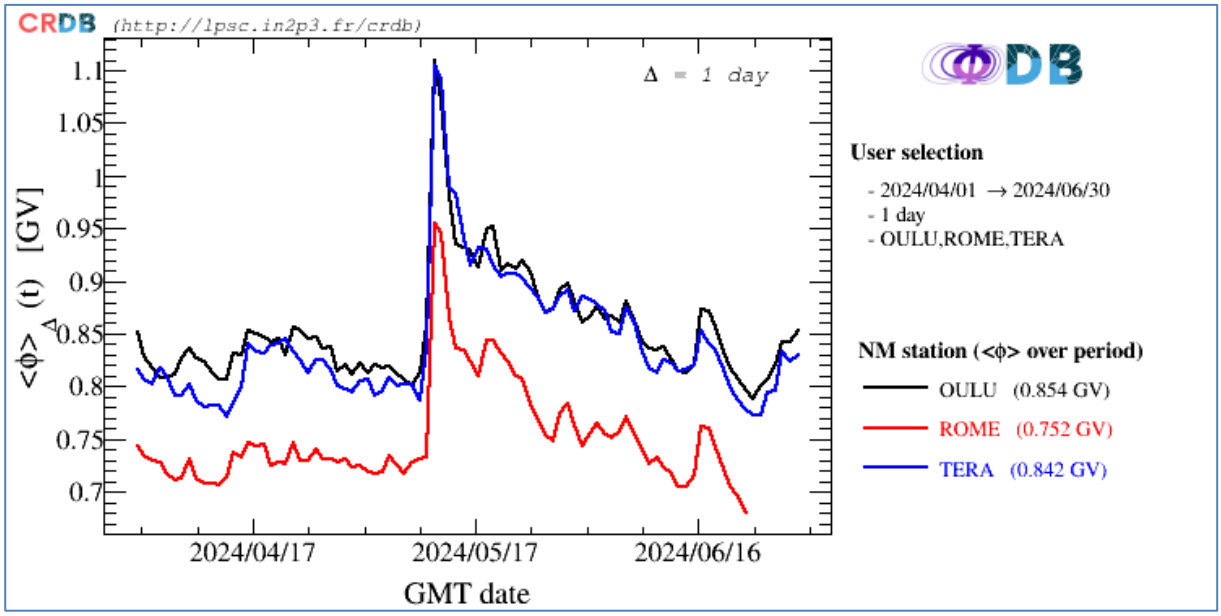

Figure 20: Modulation potentials retrieved from the Cosmic Ray Database (https://lpsc.in2p3.fr/crdb/#). These values were derived from OULU, TERA, and ROME neutron monitor data.

The comparison between the DECOS1 muon detector data [relative intensity change $\delta=(I-I_0)/I_0$ in %, with I_0 being the pre-FD muon intensity] and the simulations based on the modulation potential data for May 2024 demonstrates a strong overall agreement. Interpolating the simulation onto the experimental timestamps yields a Pearson correlation of about 0.83, confirming that the simulation successfully captures the temporal evolution and major structures of the observed cosmic ray intensity variations. The average deviation remains moderate, with a Mean Absolute Error ($MAE = \sum_{i=1}^{N}|\delta_{observed,i} - \delta_{predicted,i}|/N$) of 0.49 % to 0.52 % (i.e., corresponding to about 12 % to 13% of the total amplitude of the Forbush decrease). The reduced chi-square value of 1.6, close to unity, shows that the discrepancies are within a reasonable range given the experimental uncertainties in the relative intensity change (about 0.5 %). These results suggest that the simulation framework provides a realistic representation of the observed Forbush decrease and short-term cosmic ray modulation, although further refinement could improve amplitude matching.

4 Conclusion

A metrological methodology for quantifying the dependence of ground-level secondary cosmic radiation (SCR) on primary cosmic rays (PCR) and atmospheric parameters, specifically air pressure and temperature has been developed. Ground-based muon measurements were combined with an MCNP-based atmospheric simulation framework, incorporating measured and standard atmospheric profiles to model the production, attenuation, and propagation of SCR. Methods to decode atmospheric influences from the measured SCR count rates were explored and SCR yields per proton to establish a quantitative relationship between PCR and SCR were

determined. Validation against PARMA, EXPACS, and field campaign data confirms the model's reliability in capturing both background fluxes and their variability under geomagnetic disturbances.

By employing accurate source definitions and atmospheric profiling parameters, this methodology effectively distinguishes genuine cosmic-ray effects from atmospheric influences. Furthermore, SCR simulations using this approach can be used to support risk assessment and mitigation strategies in aviation, space exploration, and high-altitude living. They also offer a framework for understanding long-term biological consequences of repeated or chronic low-dose exposure, contributing to research in aging, evolution, and disease mechanisms.

5 Acknowledgments

The project (21GRD02 BIOSPHERE) has received funding from the European Partnership on Metrology, co-financed by the European Union's Horizon Europe Research and Innovation Programme and by the Participating States. Funded by the European Union.

6 References

Albrecht, J. et al. (2022) 'The Muon Puzzle in cosmic-ray induced air showers and its connection to the Large Hadron Collider', Astrophysics and Space Science, 367(3). doi: 10.1007/s10509-022-04054-5.

Al-Qaaod, A., Pierrard, V., Winant, A., Stolzenberg, U., Ambrazova, I., Sommer, M., Slegl, J., Solc, J., Gkikoudi, A., Georgakilas, A. G., Papayannis, A., Krasniqi, F. S., Correlation Patterns of Muon Flux with Vertical Atmospheric Profiles: Insights from Monte Carlo Simulations, In review at Journal of Geophysical Research: Space Physics; https://doi.org/10.5281/zenodo.17046809

Arunbabu, K. P., Ahmad, S., Chandra, A., Dugad, S. R., Gupta, S. K., Hariharan, B., ... & Zuberi, M. (2017). Dependence of the muon intensity on the atmospheric temperature measured by the GRAPES-3 experiment. Astroparticle Physics, 94, 22-28. http://dx.doi.org/10.1016/j.astropartphys.2017.07.002

Banjac, S., Herbst, K., and Heber, B. (2019a), 'The atmospheric radiation interaction simulator (AtRIS): Description and validation', Journal of Geophysical Research: Space Physics, 124:50–67.

Banjac, S., Herbst, K., and Heber, B. (2019b), 'On-the-fly calculation of absorbed and equivalentatmospheric radiation dose in a water phantomwith the atmospheric radiation interactionsimulator (AtRIS)', Journal of Geophysical Research: Space Physics, 124:50–67.

Chilingarian, A., & Karapetyan, T. (2011). Calculation of the barometric coefficients at the start of the 24th solar activity cycle for particle detectors of Aragats Space Environmental Center. Advances in Space Research, 47(7), 1140-1146. https://doi.org/10.1016/j.asr.2010.12.001.

Gaisser, T.K., Engel, R. and Resconi, E. (2016) Cosmic Rays and Particle Physics. Cambridge University Press. doi: https://doi.org/10.1017/CBO9781139192194.

Garrett, E. and Gregg, W. (2014) 'MCNP6 Cosmic & Terrestrial Background Particle Fluxes - Release 4' (No. LA-UR-14-24445). Los Alamos National Laboratory (LANL), Los Alamos, NM (United States).

Gleeson, L. J., & Axford, W. I. (1968). Solar modulation of galactic cosmic rays. The Astrophysical Journal, 154, 1011–1026. https://doi.org/10.1086/149822

Goorley, J.T. et al. (2013) Initial MCNP6 release overview-MCNP6 version 1.0 (No. LA-UR-13-22934). NM (United States).

Gregg, W. (2013) 'MCNP Simulations of Background Particle Fluxes from Galactic Cosmic Rays'. In Transactions of the American Nuclear Society Annual Meeting, Atlanta (Vol. 108, pp. 651-654).

Grieder, P. K. F. (2001), 'Cosmic rays at Earth. Elsevier'.

Groom, D. E., Mokhov, N. V. and Striganov, S. I. (2001) 'MUON STOPPING POWER AND RANGE TABLES 10 MeV–100 TeV', Atomic Data and Nuclear Data Tables, 78(2), pp. 183–356. doi: 10.1006/ADND.2001.0861.

Herbst, K., Muscheler, R., Heber, B. (2017), 'The new local interstellar spectra and their influence on the production rates of the cosmogenic radionuclides 10Be and 14C', J. Geophys. Res. Space Phys. 122, 23–34.

ICRU (International Commission on Radiation Units and Measurements). Fundamental Quantities and Units for Ionizing Radiation. ICRU Report 60, Bethesda, MD: International Commission on Radiation Units and Measurements, 1998.

Krasniqi, F. et al. (2022) 'PTB metrological infrastructure for the environmental dose assessment', 132(3), pp. 21–31. Available at: https://inis.iaea.org/records/pymbr-brs52 (Accessed: 6 May 2025).

Lechmann, A. et al., Muon tomography in geoscientific research – A guide to best practice, Earth-Science Reviews 222 (2021) 103842; https://doi.org/10.1016/j.earscirev.2021.103842

Maghrabi, A. H. et al. (2023) 'The Role of Atmospheric Pressure, Temperature, and Humidity on Cosmic Ray Muons at a Low Latitude Station', International Journal of Astronomy and Astrophysics, 13(3), pp. 236–258. doi: 10.4236/IJAA.2023.133014.

Mahon, D. et al. (2019) 'First-of-a-kind muography for nuclear waste characterization'. Philosophical Transactions of the Royal Society A. 2019 Jan 28;377(2137):20180048. doi: 10.1098/RSTA.2018.0048.

Mavromichalaki, H. et al. (2011) 'Applications and usage of the real-time Neutron Monitor Database', Advances in Space Research, 47(12), pp. 2210–2222. doi: 10.1016/J.ASR.2010.02.019.

McKinney, G. W. et al. (2012) 'MCNP6 Cosmic-Source Option' (No. LA-UR-12-22318). Los Alamos National Laboratory (LANL), Los Alamos, NM (United States).

Mendonça, R. R. S. et al. (2019) 'Analysis of Cosmic Rays' Atmospheric Effects and Their Relationships to Cutoff Rigidity and Zenith Angle Using Global Muon Detector Network Data'. Journal of Geophysical Research: Space Physics, 124(12), pp. 9791–9813. doi: 10.1029/2019JA026651.

Mironova, I. A. et al. (2015) 'Energetic Particle Influence on the Earth's Atmosphere', Space Science Reviews, 194(1–4), pp. 1–96. doi: 10.1007/s11214-015-0185-4.

National Oceanic and Atmospheric Administration (NOAA). (1976). U.S. Standard Atmosphere, 1976. NOAA-S/T 76-1562. U.S. Government Printing Office, Washington, D.C.; https://www.ngdc.noaa.gov/stp/space-weather/online-publications/miscellaneous/us-standard-atmosphere-1976/us-standard-atmosphere_st76-1562_noaa.pdf; Accessed: 2025-09-29.

Pierrard, V. et al. (2025) 'BIOSPHERE measurement campaign from January 2024 to March 2024 and in May 2024: Effects of the solar events on the radiation belts, UV radiation and ozone in the atmosphere', AIMS Geosciences 2025 1:117, 11(1), pp. 117–154. doi: 10.3934/GEOSCI.2025007.

Sato, T. (2015) 'Analytical model for estimating terrestrial cosmic ray fluxes nearly anytime and anywhere in the world: Extension of PARMA/EXPACS', PLoS ONE, 10(12), pp. 1–33. doi: 10.1371/journal.pone.0144679.

Sato, T. (2016) 'Analytical model for estimating the zenith angle dependence of terrestrial cosmic ray fluxes', PLoS ONE, 11(8), pp. 1–22. doi: 10.1371/journal.pone.0160390.

Thompson, L. et al. (2021) 'The use of muon radiography in safeguarding geological repositories', Safety of Nuclear Waste Disposal, 1, pp. 279–280. doi: 10.5194/sand-1-279-2021.

Tramontini, M. et al. (2019) 'Middle-Atmosphere Dynamics Observed With a Portable Muon Detector', Earth and Space Science, 6(10), pp. 1865–1876. doi: 10.1029/2019EA000655')).

Usoskin, I. G., K. Alanko-Huotari, G. A. Kovaltsov, and K. Mursula (2005), Heliospheric modulation of cosmic rays: Monthly reconstruction for 1951–2004, J. Geophys. Res., 110, A12108, https://doi.org/10.1029/2005JA011250.

Winant A. and Pierrard V., Good Practice Guide for the simulation and estimation of particle fluxes during minimum solar activity, maximum solar activity and the recent Solar Energetic Particle Events, www.euramet-biosphere.eu, 2025. https://doi.org/10.5281/zenodo.16992405

Winant, A., Pierrard, V., Botek, E. and Herbst, K. (2023) 'The Atmospheric Influence on Cosmic-Ray-Induced Ionization and Absorbed Dose Rates', Universe, 9, no. 12, p. 502. doi: 10.3390/universe9120502.

Wissmann, F. (2006) 'Variations observed in environmental radiation at ground level', Radiation Protection Dosimetry, 118, pp. 3–10. doi.org/10.1093/rpd/nci317.

Wissmann, F., Dangendorf, V. and Schrewe, U. (2005) ‘Radiation exposure at ground level by secondary cosmic radiation’, Radiation Measurements, 39(1), pp. 95–104. doi: 10.1016/J.RADMEAS.2004.03.025.